Nano Research Energy

ISSN 2791-0091 CN 10-1944/O6
https://doi.org/10.26599/NRE.2026.9120273

Research Article

Catholyte-free composite cathodes to improve the energy density of low-cost $LiMn_2O_4$-based all-solid-state lithium batteries

Zheyuan Lin[1,§], Zhenqi Gu[1,2,§], Rongcheng Zhang[1], Shiqing Sun[1], Tian Ma[1], Haosen Li[1], Yibo Niu[1], Yuanyuan Nie[1], Xianyu Liu[3], Ying Wu[1], Hongyun Ma[1], Yujun Fu[1], Junshuai Li[1], Kai Wang[1](✉), Deyan He[1](✉)

[1] School of Materials & Energy, Lanzhou University, Lanzhou 730000, China

[2] School of Materials Science and Engineering, Xihua University, Chengdu 610039, China

[3] Bailie School of Petroleum Engineering, Lanzhou City University, Lanzhou 730070, China

[§] Zheyuan Lin and Zhenqi Gu authors contributed equally to this work.

Nano Research Energy, **Just Accepted Manuscript** • https://doi.org/10.26599/NRE.2026.9120273

https://www.sciopen.com/journal/2791-0091 on Sep. 14, 2026

Just Accepted

TABLE OF CONTENTS (TOC)

Catholyte-free composite cathodes to improve the energy density of low-cost $LiMn_2O_4$-based all-solid-state lithium batteries

Zheyuan Lin, Zhenqi Gu, Rongcheng Zhang, Shiqing Sun, Tian Ma, Haosen Li, Yibo Niu, Yuanyuan Nie, Xianyu Liu, Ying Wu, Hongyun Ma, Yujun Fu, Junshuai Li, Kai Wang and Deyan He**

School of Materials & Energy, Lanzhou University, Lanzhou, Gansu 730000, China
School of Materials Science and Engineering, Xihua University, Chengdu, Sichuan 610039, China
Bailie School of Petroleum Engineering, Lanzhou City University, Lanzhou, Gansu 730070, China

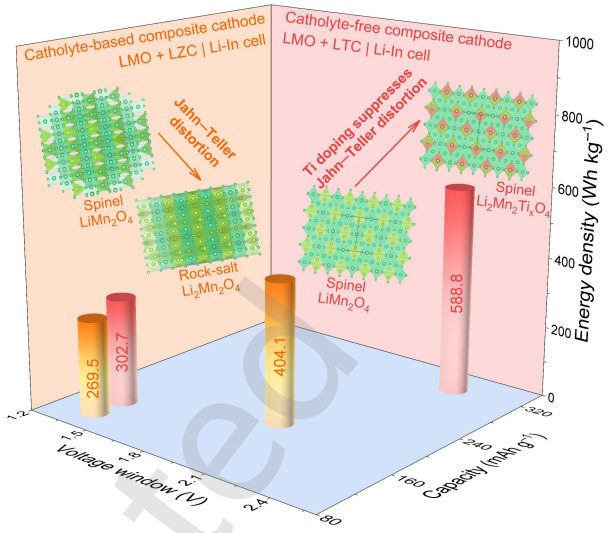

The researchers developed catholyte-free composite cathodes by replacing the inert catholyte in conventional catholyte-based composite cathodes with an active halide cathode. This strategy not only improves the energy density of low-cost $LiMn_2O_4$-based all-solid-state lithium batteries, but also extends their cycle life by suppressing Jahn-Teller distortion. The design is expected to facilitate the industrialization of high-energy-density, low-cost all-solid-state lithium batteries.

Kai Wang, https://mat.lzu.edu.cn/show_teacher/id/27.html
Deyan He, https://mat.lzu.edu.cn/show_teacher/id/3.html

Nano Research Energy

ISSN 2791-0091 (print); 2790-8119 (online)
https://doi.org/10.26599/NRE.2026.9120273

Research Article

Catholyte-free composite cathodes to improve the energy density of low-cost $LiMn_2O_4$-based all-solid-state lithium batteries

Zheyuan Lin[1,§], Zhenqi Gu[1,2,§], Rongcheng Zhang[1], Shiqing Sun[1], Tian Ma[1], Haosen Li[1], Yibo Niu[1], Yuanyuan Nie[1] Xianyu Liu[3], Ying Wu[1], Hongyun Ma[1], Yujun Fu[1], Junshuai Li[1], Kai Wang[1] (✉), and Deyan He[1] (✉)

[1] *School of Materials & Energy, Lanzhou University, Lanzhou 730000, China*
[2] *School of Materials Science and Engineering, Xihua University, Chengdu 610039, China*
[3] *Bailie School of Petroleum Engineering, Lanzhou City University, Lanzhou 730070, China*
[§] *Zheyuan Lin and Zhenqi Gu authors contributed equally to this work.*

Received: 5 June 2026 / **Revised:** 25 August 2026 / **Accepted:** 5 September 2026

ABSTRACT

The cost-effective manganese-based spinel oxide $LiMn_2O_4$ (LMO) is a promising cathode material for large-scale applications in all-solid-state lithium batteries (ASSLBs). However, the gravimetric energy density of all-solid-state lithium pouch batteries (ASSLPBs) with conventional catholyte-based composite cathodes containing LMO is only about 256.8 Wh kg^{-1}, far below the target value of 500 Wh kg^{-1}, and the Jahn-Teller distortion leads to poor cycling stability. To address this issue, the study proposes replacing the inert catholyte with an active halide cathode Li_3TiCl_6 (LTC) and combining it with the low-cost LMO cathode to form a design of catholyte-free composite cathodes. During deep charge and discharge cycles, the Ti in LTC inserts into the lattice of LMO, which both improves the discharge specific capacity of the catholyte-free composite cathode to 316.3 mAh g^{-1} and extends the cycling life by reducing the Jahn-Teller distortion. As a result, the gravimetric energy density of the ASSLPB with the catholyte-free composite cathode reaches 588.8 Wh kg^{-1}, which is 2.3 times higher than that of conventional catholyte-based composite cathodes. Therefore, the design of the catholyte-free composite cathode effectively solves the issues of insufficient energy density and short cycling life of low-cost LMO cathodes in large-scale applications.

KEYWORDS

all-solid-state lithium batteries, manganese-based spinel cathode $LiMn_2O_4$, catholyte-free composite cathode, catholyte-based composite cathode, energy density

1 Introduction

All-solid-state lithium batteries (ASSLBs) are next-generation energy storage devices with high energy density and inherent safety [1-4]. However, achieving a balance between low cost and high energy density remains challenging in the large-scale application of ASSLBs [5]. This challenge arises from the high cost of cobalt-based oxide cathode materials, which offer high energy density, and the relatively low energy density of cost-effective manganese-based oxide cathode materials [6]. Furthermore, in conventional ASSLB configurations that utilize these undeformable oxide cathode materials, approximately 25 wt% of a deformable solid-state electrolyte (SSE), such as sulfides [7-9] or halides [10-12], is incorporated into the composite cathode as an inert catholyte to facilitate Li^+ transport [5, 8]. This addition further reduces the theoretical energy density of the conventional catholyte-based composite cathode.

The cost and energy density of ASSLBs primarily depend on the oxide active material in the conventional catholyte-based composite cathode [13]. Commercial cobalt-based layered cathode material $LiCoO_2$, for example, offers a theoretical gravimetric energy density of 560 Wh kg^{-1} (140 mAh g^{-1} × 4 V *vs.* Li/Li^+) [9, 14]. However, due to the limited availability of cobalt, which has an abundance of only 30 ppm, and a high development cost of approximately \$33 kg^{-1}, the material cost of $LiCoO_2$ is \$55 kg^{-1} [13]. To enhance energy density while reducing material costs, low-cobalt, high-nickel ternary oxide cathode materials, such as $LiNi_{0.8}Mn_{0.1}Co_{0.1}O_2$, have been developed, typically offering a theoretical energy density of 780 Wh kg^{-1} (200 mAh g^{-1} × 3.9 V *vs.* Li/Li^+) [9, 15]. Despite the relatively high nickel abundance of 90 ppm, its development cost remains

Address correspondence to kai Wang, kwang@lzu.edu.cn; Deyan He, hedy@lzu.edu.cn

around \$20 kg^{-1}, resulting in an overall high material cost [13]. Furthermore, the high nickel content compromises the thermal stability and high-voltage cycle life of the material. In contrast, manganese (Mn) is a more abundant element, with a natural abundance of 1100 ppm, and the cost of manganese metallurgy ores is only \$1.81 kg^{-1}, enabling manganese-based products to achieve higher annual mineral output and better economic efficiency [13, 16-18]. Although the theoretical gravimetric energy density of manganese-based spinel oxide $LiMn_2O_4$ (LMO) is comparatively lower at 480 Wh kg^{-1} (120 mAh g^{-1} × 4 V *vs.* Li/Li^+) [7], its material cost is much lower, at just \$12 kg^{-1} [13]. One promising strategy to improve the energy density of LMO is to dope it with elements such as Al [19], Mg [20], Fe [21], and Ti [19, 22], which reduce the Jahn-Teller distortion and Mn dissolution, enabling a wider charge-discharge voltage window and improved specific capacity [23-25]. Considering both its economic benefits and energy density, manganese-based spinel oxide LMO shows significant potential for large-scale applications in ASSLBs.

Additionally, the deformable catholyte in conventional catholyte-based composite cathodes also plays a crucial role in determining the overall energy density and cost of ASSLBs [5, 8]. The most commonly used sulfide-based SSE in these systems, Li_6PS_5Cl (LPSCl), is expensive, costing more than \$195 kg^{-1} [13], while halide catholytes containing rare earth elements (Li_3YCl_6) are priced above \$196.3 kg^{-1} [26]. Currently, low-cost zirconium-based halides, such as Li_2ZrCl_6 (LZC) [15] and $Li_{1.75}ZrCl_{4.75}O_{0.5}$ [26], which cost approximately \$10.7 kg^{-1} and \$11.6 kg^{-1}, respectively, offer better cost-effectiveness. However, these materials, though inexpensive, do not contribute to the electrochemical capacity of the composite cathode and their inclusion further reduces the overall energy density. Notably, recent developments have introduced low-cost, non-rare earth-based deformable halides with redox activity as viable cathode materials for ASSLBs. For example, Li_3TiCl_6 (LTC) can provide a theoretical gravimetric energy density of up to 477.0 Wh kg^{-1} and exhibits room-temperature ionic conductivity of up to 1 mS cm^{-1}, enabling rapid Li^+ transport [27]. Other redox-active deformable halides, such as $LiFeCl_3$ [28], $Li_{1.3}Fe_{1.2}Cl_4$ [1], Li_2FeCl_4 [29], Li_3VCl_6 [30], and $Li_{2.9}Fe_{0.9}Zr_{0.1}Cl_6$ [31] offer theoretical gravimetric energy densities of 912, 529.3, 369.6, 240.0, and 214.2 Wh kg^{-1}, respectively. However, their room temperature ionic conductivity is below 0.2 mS cm^{-1} [1, 28-31], which limits their performance in terms of fast Li^+ transport. Therefore, the use of deformable halide cathode materials, which both facilitate fast Li^+ transport and provide high energy density, offers a feasible strategy to enhance the energy density of ASSLBs without incurring additional costs.

Here, we have developed a catholyte-free composite cathode by combining low-cost manganese-based spinel oxide LMO with the deformable halide cathode LTC. Compared to conventional catholyte-based composite cathodes using LZC as an inert catholyte, the catholyte-free composite cathode shows a significant increase in discharge specific capacity in ASSLBs. Specifically, for the LMO + LTC | Li-In cell with the catholyte-free composite cathode, Ti atoms can be inserted into the 16*c* sites of LMO during deep charge-discharge cycles. This insertion reduces Jahn-Teller distortion, ensuring that the cell maintains a discharge specific capacity of 97.5 mAh g^{-1} after 500 cycles, whereas conventional catholyte-based composite cathodes lose their charge-discharge capability due to Jahn-Teller distortion. Based on energy density estimates, the gravimetric energy density of all-solid-state lithium pouch batteries (ASSLPBs) assembled with the catholyte-free composite cathode is more than twice that of the conventional catholyte-based composite cathode, reaching 588.8 Wh kg^{-1}. The design of the catholyte-free composite cathode thus provides a feasible solution for enhancing the energy density of low-cost manganese-based spinel oxide LMO in large-scale applications.

2 Result and discussion

The structure of the catholyte-free composite cathodes is similar to that of the conventional catholyte-based composite cathodes, with the main difference being the replacement of the inert catholyte with an active halide cathode. As a result, the active halide cathode not only performs the role of the inert catholyte but also ensures a solid–solid physical contact interface due to its excellent deformability and high ionic conductivity, facilitating fast Li^+ transport within the composite cathode while contributing additional capacity. To construct the catholyte-free composite cathode, high-purity and high-crystallinity LMO and LTC were selected for this study. X-ray diffraction (XRD) refinement [32, 33] results indicate that LMO exhibits the spinel structure with a space group of *Fd3m* (Figure 1(a)). The crystal structure is characterized by MnO_6 octahedra, each composed of one Mn atom (occupying 16*d* sites) and six O atoms (occupying 32*e* sites), forming a three-dimensional framework. LiO_4 tetrahedra, consisting of one Li atom (occupying 8*a* sites) and four O atoms, are located this framework (Fig. S1; Table S1) [13]. This structure provides a three-dimensional Li^+ transport pathway, with a tetrahedral–octahedral–tetrahedral arrangement that promotes rapid Li^+ migration. Similarly, XRD results show that LTC displays a layered structure with a space group of *C2/m* (Fig. 1(b)). The crystal structure is characterized by $TiCl_6$ octahedra, composed of one Ti atom (occupying 2*a* and 4*g* sites) and six Cl atoms (occupying 4*i* and 8*j* sites), forming a layered two-dimensional framework. $LiCl_6$ octahedra, composed of one Li atom (occupying 2*d* and 4*h* sites) and six Cl atoms, are positioned at the interlayer of this framework (Fig. S2; Table S2) [27]. In contrast to the three-dimensional transport pathway in LMO, the one-dimensional transport pathway (octahedral–octahedral–octahedral) in LTC offers enhanced Li^+ migration [2]. Consequently, LTC exhibits a room-temperature ionic conductivity of up to 1.01×10^{-3}

S·cm^{-1}, while its electronic conductivity is significantly lower, at 3.04 × 10^{-7} S·cm^{-1} (Fig. S3).

When LMO and LTC are mixed in a 70:30 mass ratio, XRD refinement results show no significant impurity peaks, indicating that no substantial side reactions occur between the two materials (Fig. 1(c)). Scanning electron microscopy (SEM) images reveal that both LMO and LTC particles are irregular in shape, with particle sizes of approximately 5 μm (Fig. 1(d), 1(e)). Upon mixing LMO, LTC, and carbon black, and cold-pressing the mixture at 350 MPa to prepare the catholyte-free composite cathode, energy dispersive spectroscopy (EDS) results under Ar protection [34] indicate that LMO particles retain their 5 μm size (Fig. 1(f), 1(g)). However, the LTC particles exhibit significant deformation, making it challenging to discern whether they remained as distinct particles in the EDS signal (Fig. 1(h)). This behavior is one of the key reasons for selecting LTC as the substitute for the inert catholyte in this study. Previous research had shown that LTC undergoes significant deformation under 350 MPa cold-press conditions, resulting in a relative density of up to 86.1% for the molded pellet [27]. This ensures that the catholyte-free composite cathode maintains a solid–solid physical contact interface similar to that of conventional catholyte-based composite cathodes. Additionally, the uniformly distributed carbon black enhances the electronic conductivity of the catholyte-free composite cathode (Fig. 1(i)).

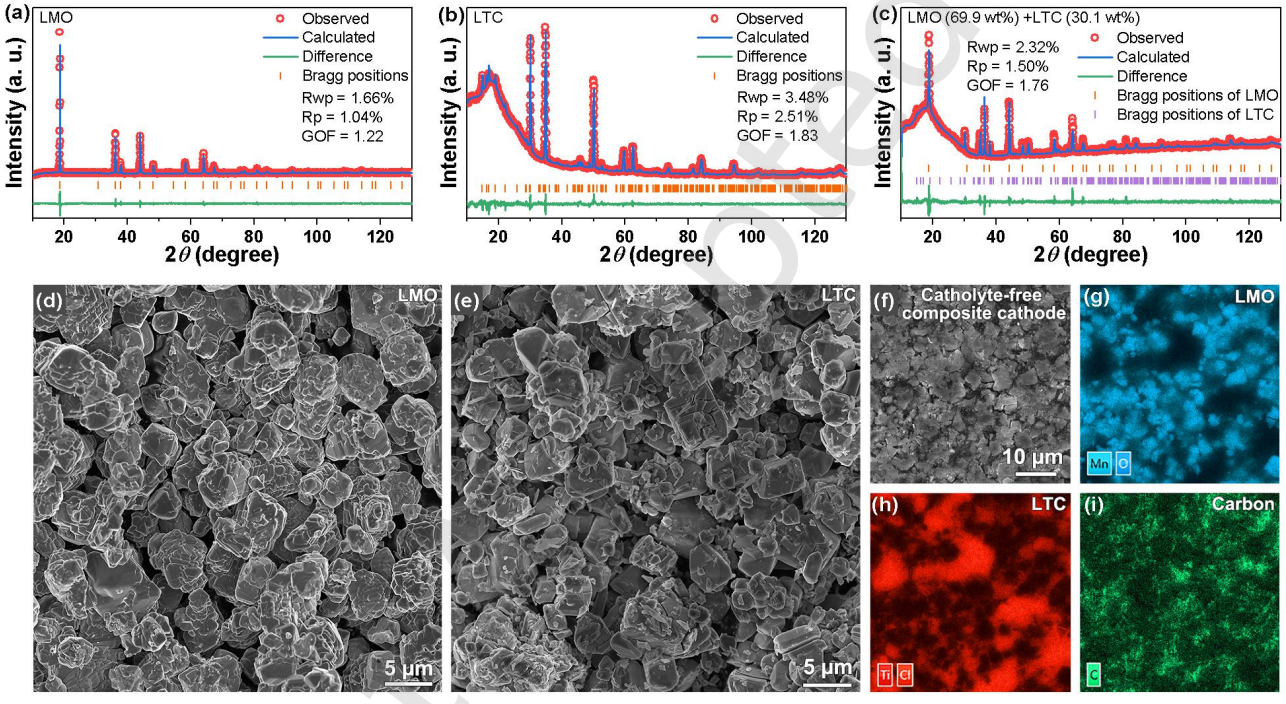

Figure 1. Structure of the catholyte-free composite cathode (LMO + LTC). (a–c) Refined XRD patterns of the LMO (a), LTC (b), and composite cathode (c). (d–f) SEM images of the LMO (d), LTC (e), catholyte-free composite cathode (f). (g–i) EDS mapping results of the catholyte-free composite cathode.

Although both LMO and LTC can undergo reversible charge and discharge cycles when used individually as cathode materials in ASSLBs, it remains to be verified whether they will still perform effectively when combined in a catholyte-free composite cathode. To investigate this, ASSLBs were assembled with LMO, LTC, and carbon black as the catholyte-free composite cathode, LZC as the SSE, and a Li-In alloy as the anode. Notably, to minimize the impact of potential side reactions between LZC and Li-In alloy on the performance of the catholyte-free composite cathode, an LPSCl interlayer was introduced between LZC and Li-In alloy.

The LMO + LTC | Li-In cell first exhibits a charging plateau at approximately 3.2 V *vs.* Li/Li$^+$, corresponding to the Ti^{3+}/Ti^{4+} redox reaction of LTC, during the charging process from 2.92 V to 4.32 V *vs.* Li/Li$^+$ (Figure 2(a) and Fig. S4). Subsequently, charging plateaus appear at around 4.0 V and 4.1 V *vs.* Li/Li$^+$, which are attributed to the $Li_xMn_2O_4$ (0.5 < x < 1, phase I) and $Li_xMn_2O_4$ (0 < x < 0.5, phase II), respectively (Fig. 2(a) and Fig. S4). At 4.32 V *vs.* Li/Li$^+$, LMO is fully transformed into Mn_3O_4. During the subsequent discharge process from 4.32 V to 2.92 V *vs.* Li/Li$^+$, distinct discharge plateaus corresponding to both LMO and LTC are observed, indicating the reversibility of the redox reactions of both materials (Fig. 2(a) and Fig. S4). The LMO + LTC | Li-In cell demonstrates a charge-specific capacity of 150.1 mAh g^{-1} and a discharge-specific capacity of 136.5 mAh g^{-1}, with an initial Coulombic efficiency of 91.0% (Fig. 2(a)). Within the 2.92–4.32 V *vs.* Li/Li$^+$ voltage window, these specific capacities are notably higher than those of the LMO + LZC | Li-In cell, which is based on a conventional catholyte-based composite cathode (120.0 mAh g^{-1} and 107.7 mAh g^{-1}, respectively; Fig. 2(d)). These values also exceed the average specific capacities reported for conventional catholyte-based composite cathodes in ASSLBs (104.0 mAh g^{-1}) [10, 12, 35-42]. To ensure a fair comparison, only the mass of LMO is considered as the active material when calculating the specific capacity.

Consequently, the ASSLB with the catholyte-free composite cathode achieves an approximately 26.7% higher discharge specific capacity than its catholyte-based counterpart within the 2.92–4.32 V *vs.* Li/Li^+ range (Fig. 2(a), 2(d)).

The LMO + LTC | Li-In cell based on the catholyte-free composite cathode also demonstrates good rate capability. At current rates of 0.1C, 0.2C, 0.3C, 0.4C, 0.5C, and 1C, it delivers average discharge specific capacities of 129.8, 110.2, 94.9, 81.9, 71.5, and 40.4 mAh g^{-1}, respectively (Fig. 2(b)). In comparison, the LMO + LZC | Li-In cell based on the conventional catholyte-based composite cathode shows discharge specific capacities of 100.1, 88.9, 82.3, 77.4, 73.9, and 59.5 mAh g^{-1} at the corresponding rates (Fig. 2(e)). Although the LMO + LTC | Li-In cell delivers higher discharge capacities, its rate performance is slightly inferior, likely due to the relatively large interfacial resistance between LMO and LTC in the catholyte-free composite cathode. However, when the current rate was reduced from 1C back to 0.1C, the charge and discharge capacities are fully recovered. After 100 cycles, while the capacity retention of the LMO + LTC | Li-In cell is lower than that of the LMO + LZC | Li-In cell, it still maintains a relatively high discharge specific capacity (Fig. 2(c), 2(f)). Long-term cycling performance analysis using dQ/dV curves reveals characteristic peaks corresponding to both single-active-material and dual-active-material electrochemical processes (Fig. 2(c), 2(f)).

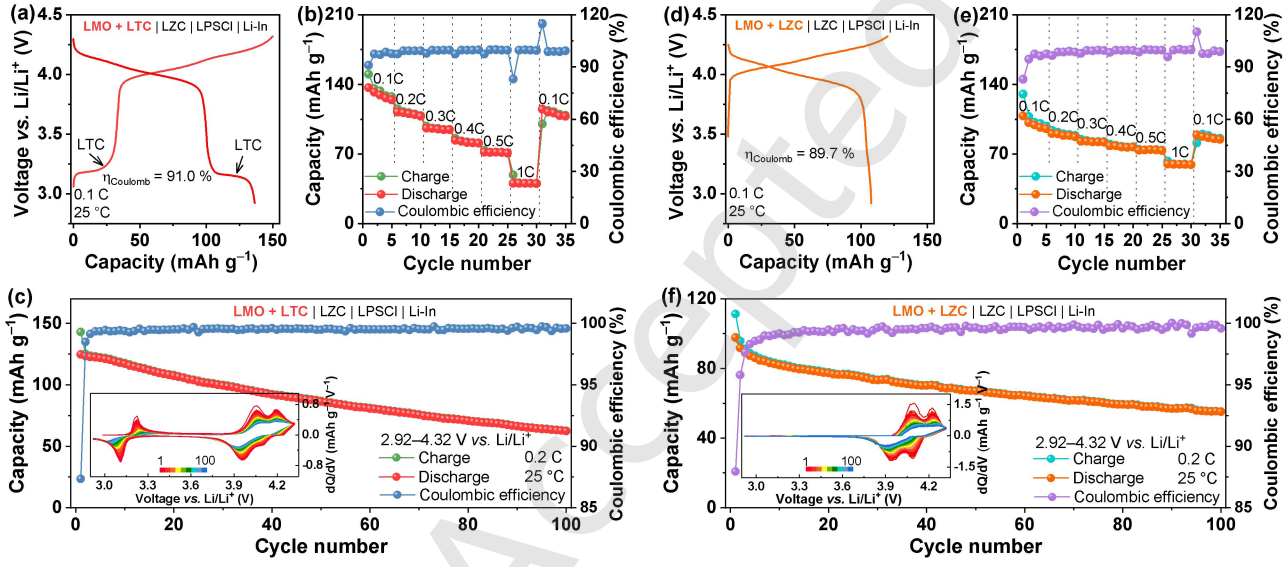

Figure 2. Electrochemical performances of the ASSLBs with catholyte-based and catholyte-free composite cathodes. (a–c) Initial charge/discharge curve (a), rate capability (b), long-term cycling performance and dQ/dV curve (c) of LMO + LTC | Li-In cells. (d–f) Initial charge/discharge curve (d), rate capability (e), long-term cycling performance and dQ/dV curve (f) of LMO + LZC | Li-In cells.

Neither the ASSLBs based on the conventional catholyte-based composite cathode nor those based on the catholyte-free composite cathode exhibit satisfactory long-term cycling performance (Fig. 2(c), 2(f)). Previous researches have shown that LMO could undergo interfacial side reactions with sulfide catholyte [13, 41], which have severely degraded the long-term cycling performance of ASSLBs. To determine whether interfacial reactions are the primary cause of the performance degradation observed in this study, XRD characterization was conducted on the composite cathodes of the LMO + LTC | Li-In and LMO + LZC | Li-In cells after 100 cycles. The results show that, apart from the characteristic diffraction peaks of LMO, LTC, and LZC, no additional peaks are detected in the XRD patterns (Figure 3(a), 3(f)); only the full width at half maximum (FWHM) of the peaks increased as cycling proceeded (Figs. S5, S6). This indicates that neither LZC nor LTC undergoes significant side reactions with LMO. Therefore, the long-term performance degradation of both the LMO + LTC | Li-In and LMO + LZC | Li-In cells is unlikely to originate from interfacial chemical reactions.

Additionally, Mn diffusion during charge–discharge cycling has been reported as another critical factor contributing to the performance degradation of ASSLBs based on conventional catholyte-based composite cathodes, particularly those using sulfide catholytes [13, 20, 43, 44]. To further investigate this potential degradation mechanism, the microstructure and elemental distribution of the composite cathodes in the LMO + LTC | Li-In and LMO + LZC | Li-In cells were analyzed after 100 cycles. SEM and EDS results under Ar protection [34] reveal that, compared to the pristine state, where a clear interface exists between LMO particles and LTC (Fig. 1(g), 1(h)), noticeable diffusion of Mn from LMO into LTC occurs after cycling (Fig. 3(b), 3(c)). Similarly, after cycling, the interface between LMO and LZC becomes less distinct, and the LMO particles lose their original morphological features (Fig. 3(g), 3(h)). Mn diffusion from the LMO cathode is likely accompanied by oxygen loss, which increases the interfacial resistance between LMO and LTC or LZC, ultimately leading to a deterioration in electrochemical performance.

To further validate this degradation mechanism, distribution of the relaxation time (DRT [45, 46]) was performed on the LMO + LTC | Li-In and LMO + LZC | Li-In cells before and after cycling. During the second charge–discharge cycle, both cells exhibit relatively large

impedance components within the 0–2 s region, which corresponds to the surface electron-transfer processes of LMO with LTC or LZC (Fig. 3(d), 3(i) and Figs. S7, S8). Note that although the fitting accuracy of DRT in the high-frequency region was not as good as that in the low-frequency region (Fig. S9), this did not affect the analysis of various interfacial impedances, which mainly originate from the low-frequency region. In contrast, the interfacial impedance between LMO and LTC or LZC in the −3 to 0 s region remains relatively small. After 100 cycles, however, the impedance in the −3 to 0 s region increases markedly, further confirming that Mn diffusion and oxygen loss lead to enhanced interfacial resistance, thereby impairing the electrochemical performance of the cells (Fig. 3(e), 3(j) and Figs. S10, S11). Notably, during the second cycle, the charge-transfer resistance of the LMO + LTC | Li-In cell is primarily concentrated at the transition between the LMO and LTC charge–discharge plateaus (Fig. 3(d)). After 100 cycles, in addition to the increased interfacial resistance between LMO and LTC, the charge-transfer resistance shifts to higher voltage regions (Fig. 3(i)). These observations further demonstrate that structural degradation of LMO is the primary cause of performance decay in both the LMO + LTC | Li-In and LMO + LZC | Li-In cells.

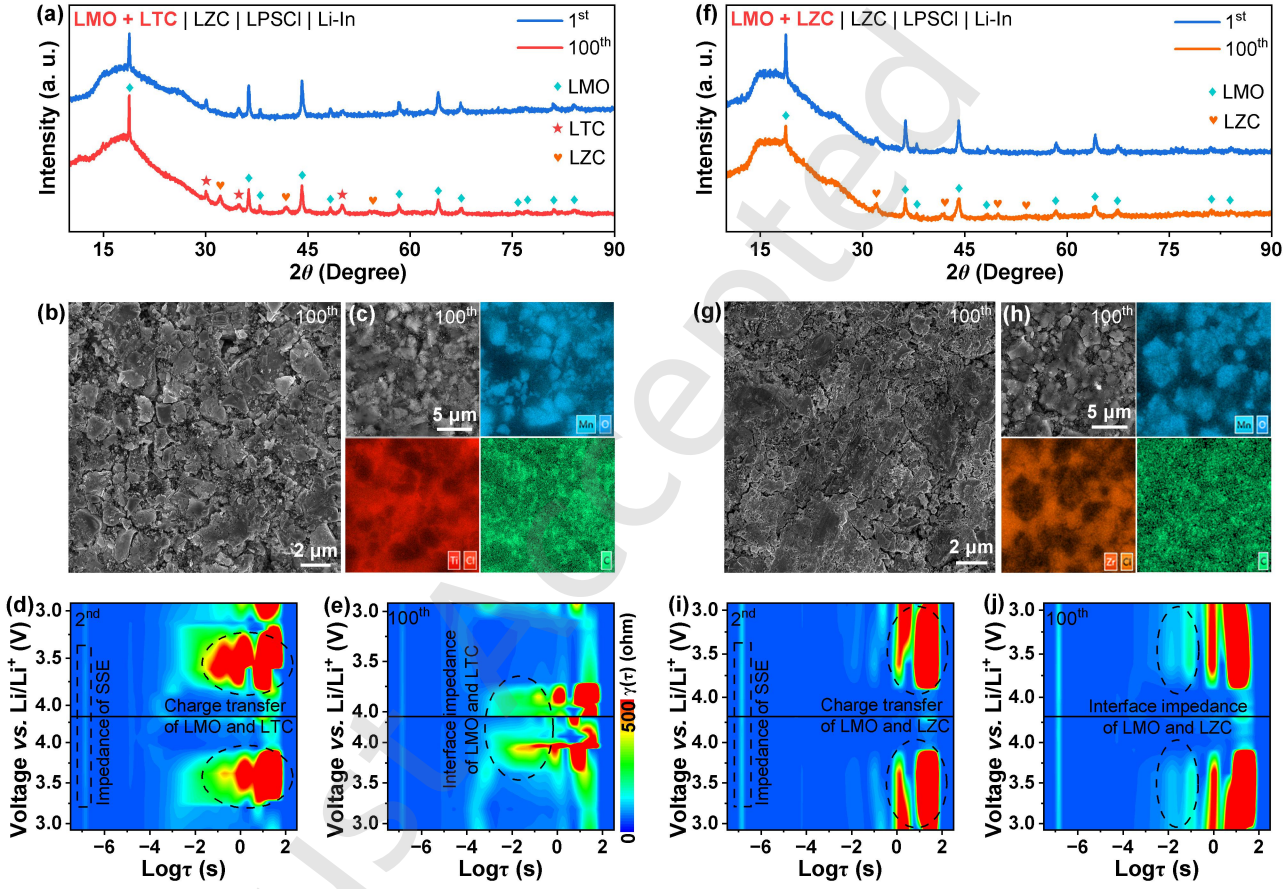

Figure 3. Electrochemical stability of the ASSLBs with catholyte-based and catholyte-free composite cathodes. (a, f) XRD patterns of composite cathode after 1st (a) and 100th (f) cycling for the LMO + LTC | Li-In and LMO + LZC | Li-In cells, respectively. (b, c) SEM image (b) and EDS mapping result (c) after 100th cycling of LMO + LTC | Li-In cell. (d, e) DRT analysis at the 2nd cycle (d) and the 100th cycle (e) of LMO + LTC | Li-In cells. (g, h) SEM image (g) and EDS mapping result (h) after 100th cycling of LMO + LZC | Li-In cell. (i, j) DRT analysis at the 2nd cycle (i) and the 100th cycle (j) of LMO + LZC | Li-In cells. Note that the contour scale bars in (d–j) are kept consistent.

Typically, the operating voltage window of ASSLBs based on LMO cathode materials is limited between 3.0 and 4.3 V *vs.* Li/Li^+ to avoid Jahn-Teller distortion and to maintain structural stability.[13, 19, 25] When the discharge voltage drops below 3.0 V *vs.* Li/Li^+, the LMO + LZC | Li-In cell shows a discharge plateau at 2.8 V *vs.* Li/Li^+, corresponding to the $Li_xMn_2O_4$ ($1 < x < 2$) phase (Figure 4(a), 4(b)). During this process, the redox reaction between Mn^{3+} and Mn^{4+} follows an equimolar transformation, where Mn^{3+} converts to (1+x) Mn^{3+} and (1-x) Mn^{4+} [13]. Mn^{3+} is a high-spin ion with an electron configuration of $t_{2g}^3e_g^1$, making it a Jahn-Teller ion, while Mn^{4+} is a low-spin ion, not a Jahn-Teller ion, with the electron configuration of $t_{2g}^3e_g^0$ [13, 25]. As the lithiation process continues and Mn^{3+} accumulates to more than half of the total manganese content, Li^+ in the spinel LMO structure migrate from the LiO_4 tetrahedral 8*a* sites to the octahedral sites, forming the ordered rock-salt phase $Li_2Mn_2O_4$ (Fig. S12) [13]. However, the phase transition from the spinel to the rock-salt structure is partially irreversible, and the formation of $Li_2Mn_2O_4$ significantly hinders Li^+ transport and increases interfacial resistance, ultimately leading to a decline in the cycling performance of ASSLBs based on LMO cathodes. The long-term cycling data for the LMO + LZC | Li-In cell validate

the detrimental impact of Jahn-Teller distortion on cell performance (Fig. 4(g)). After 100, 200, and 500 cycles, the discharge specific capacity decreases to 68.3, 29.3, and 6.4 mAh g^{-1}, corresponding to capacity retentions of 48.6%, 20.9%, and 4.6%, respectively (Fig. 4(g)).

The LMO + LTC | Li-In cell exhibits an additional discharge plateau below 2.2 V *vs.* Li/Li^+, corresponding to the Ti^{3+} to Ti^{2+} redox transition (Fig. 4(d), 4(e)) when the discharge voltage drops below 3.0 V *vs.* Li/Li^+, alongside the LMO plateau (Fig. S13). At 2.02 V *vs.* Li/Li^+, the discharge specific capacity reaches an impressive 316.3 mAh g^{-1}, with an initial Coulombic efficiency of 218.8% (Fig. 4(d)). Even at 1.62 V *vs.* Li/Li^+, the discharge specific capacity further increased to 374.7 mAh g^{-1}, while maintaining good cycling stability (Fig. S14). Notably, when the LMO + LTC | Li-In cell is charged and discharged within the voltage range of 2.02–4.32 V *vs.* Li/Li^+, the dQ/dV curve in the second cycle exhibits a distinct peak at 3.9 V *vs.* Li/Li^+ (Fig. 4(e)), which is difficult to detect in other cells, particularly since this peak does not appear in the dQ/dV curve of first cycle (Fig. 2(c), 2(f), and 4(b)). In other words, it is only after the LMO + LTC | Li-In cell undergoes charge-discharge cycling within the 2.92–2.02 V *vs.* Li/Li^+ range that the electrochemical reaction between LMO and LTC likely generates an additional voltage plateau at 3.9 V *vs.* Li/Li^+. The appearance of this plateau causes the discharge specific capacity of the cell to exceed the rated capacity of LMO + LTC (Fig. 4(d)), and also results in the LMO + LTC | Li-In cell outperforming the LMO + LZC | Li-In cell in rate performance (Fig. 4(c), 4(f)). More importantly, the LMO + LTC | Li-In cell, at a 0.2C rate, shows an initial discharge specific capacity of 267.7 mAh g^{-1} between 2.02–4.32 V *vs.* Li/Li^+. After 100, 200, and 500 cycles, the discharge specific capacities are 156.3, 127.3, and 97.5 mAh g^{-1}, corresponding to capacity retentions of 58.4%, 47.6%, and 36.4%, respectively (Fig. 4(g)). The experimental results indicate that, due to Jahn-Teller distortion, catholyte-based composite cathodes based on LMO undergo rapid degradation during cycling, whereas the performance of catholyte-free composite cathodes is significantly improved. In the long-term cycling dQ/dV curve of the LMO + LZC | Li-In cell, the characteristic peak of LMO disappears rapidly due to Jahn-Teller distortion (Fig. S15). In contrast, the long-term cycling dQ/dV curve of the LMO + LTC | Li-In cell shows that the characteristic peak of LMO does not disappear, while the LTC peak vanishes (Fig. S16). This suggests that Ti^{2+} ions in the LTC cathode migrate into the LMO lattice within the 2.92–2.0 V *vs.* Li/Li^+ range, alleviating the effects of Jahn-Teller distortion on LMO.

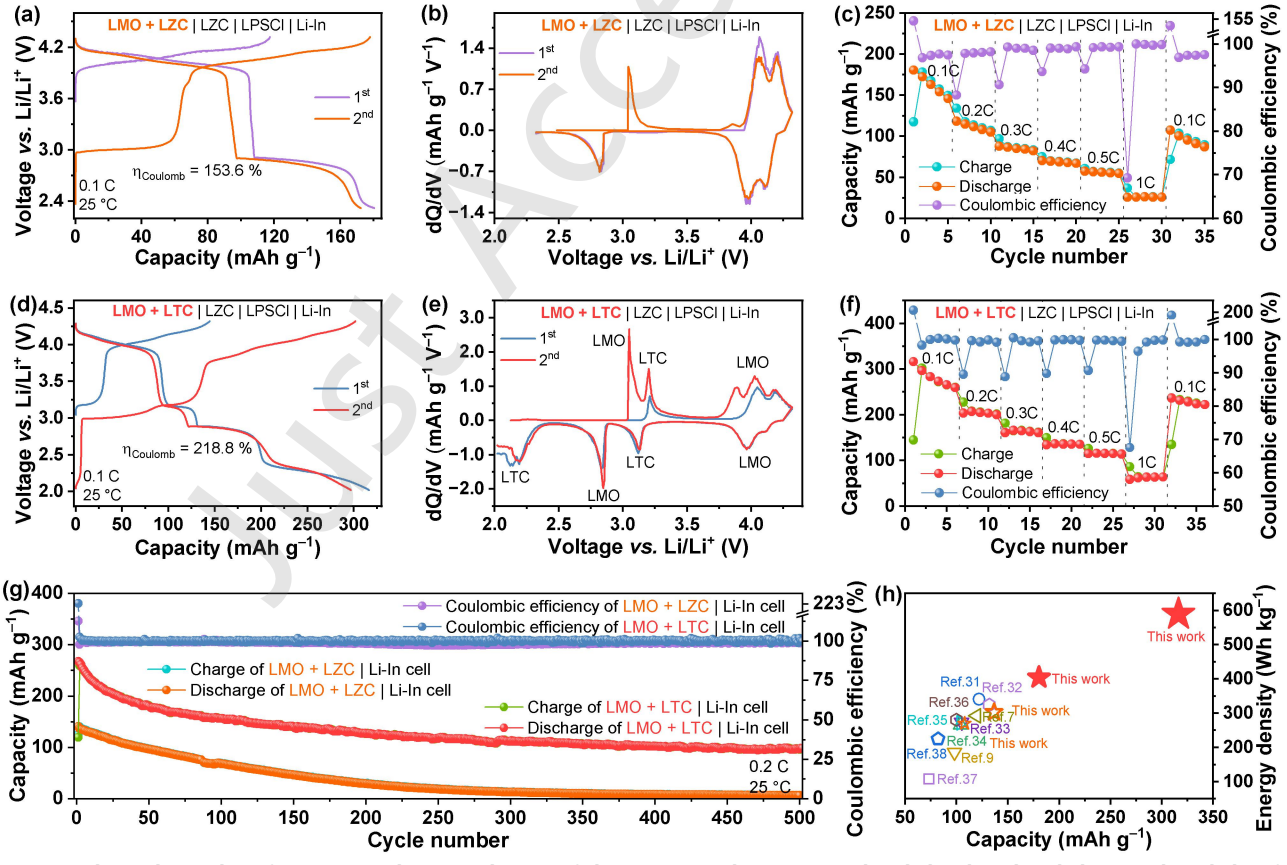

Figure 4. Electrochemical performances and energy density of the ASSLBs with conventional catholyte-based and those with catholyte-free composite cathodes. (a–c) Charge/discharge curves (a), dQ/dV curves (b), rate capability (c) of LMO + LZC | Li-In cells. (d–f) Charge/discharge curves (d), dQ/dV curves (e), rate capability (f) of LMO + LTC | Li-In cells. (g) Long-term cycling performance. (h) Estimated gravimetric/volumetric energy density values for ASSLPBs based on the catholyte-based and catholyte-free composite cathodes.

After deep charge and discharge cycles, the initial discharge specific capacity of the ASSLB based on the

catholyte-free composite cathode is 316.3 mAh g^{-1} (Fig. 4(d)), which is approximately 1.8 times that of the conventional catholyte-based composite cathode (180.5 mAh g^{-1}) (Fig. 4(a)). Additionally, the suppression of Jahn-Teller distortion contributes to the enhanced long-term cycling performance of the battery. To estimate the theoretical energy densities of the ASSLPBs based on the catholyte-free and catholyte-based composite cathodes, the experimental data were used for calculations in the SolidPAC software [47]. Because the catholyte-free and catholyte-based composite cathodes use LTC and LZC, respectively, as the sole catholytes, their comparable deformability enables consistent catholyte contents. Although the catholyte-free composite cathode contains more high-capacity active material and thus offers higher theoretical energy density (Table S3), solid–solid contact and Li-ion transport must also be considered. In these estimations, the composite cathode ratio is LMO:LZC:C:PTFE = 70:25:3:2 [48], the thickness of the LZC SSE film is 25 μm,[8] the anode is lithium metal with an N/P ratio of 1.2 [49], and the composite cathode loading is 6 mg cm^{-2} (Table S4) [9]. The energy density values reported in other research were estimated using similar battery parameters (Table S5). The results show that the gravimetric energy density of the ASSLPB with a conventional catholyte-based composite cathode (LZC-based) is 269.6 Wh kg^{-1} at 2.92–4.32 V *vs.* Li/Li^+ and 404.1 Wh kg^{-1} at 2.32–4.32 V *vs.* Li/Li^+ (Fig. 4(h)). The average gravimetric energy density of ASSLPBs reported in other researches (using various SSEs and working voltages of 3.0–4.3 V *vs.* Li/Li^+) is 256.8 Wh kg^{-1} (Table S6) [10, 12, 35-42]. In contrast, the gravimetric energy density of the ASSLPB with a catholyte-free composite cathode (LTC-based) is 302.7 Wh kg^{-1} at 2.92–4.32 V *vs.* Li/Li^+ and 588.8 Wh kg^{-1} at 2.02–4.32 V *vs.* Li/Li^+ (Fig. 4(h)). In addition, whether only the mass of the oxide active material or the mass of the entire composite cathode should be considered when calculating the theoretical energy density was further examined. When only the mass of LMO was considered, the calculated theoretical gravimetric energy density of the catholyte-based composite cathode cell was 270.3 Wh kg^{-1} (Table S7); when the mass of the entire composite cathode was considered, this value decreased to 258.2 Wh kg^{-1} (Table S7). Similarly, for the catholyte-free composite cathode, the theoretical gravimetric energy densities calculated based on the mass of LMO and the mass of the entire composite cathode were 326.0 Wh kg^{-1} and 312.2 Wh kg^{-1}, respectively (Table S7). Therefore, considering only the mass of LMO may lead to a 4.22% overestimation of the gravimetric energy density, while the volumetric energy density remains unchanged (Table S7, S8). However, for catholyte-based composite cathodes, calculating the energy density based on the mass of LMO is reasonable. Therefore, to facilitate comparison with catholyte-containing composite cathodes, this work also adopts the calculation method in which only the mass of LMO is considered when calculating the energy density of catholyte-free composite cathodes. It is worth noting that when the charge–discharge voltage window of the LMO + LTC | Li-In cell is 1.62–4.32 V *vs.* Li/Li^+, it can deliver an even higher specific capacity, with gravimetric and volumetric energy densities as high as 670.0 Wh kg^{-1} and 1080.1 Wh L^{-1}, respectively (Table S8). Therefore, compared with the conventional catholyte-based composite cathode, the gravimetric energy density of the ASSLPB with the catholyte-free composite cathode is increased by a factor of 2.3, surpassing the energy density of most cobalt-based oxide cathodes for the first time.

To further elucidate the origin of the distinct long-term cycling behaviors observed for ASSLBs with conventional catholyte-based and catholyte-free composite cathodes under deep charge/discharge conditions, scanning transmission electron microscopy (STEM) was employed to characterize the composite cathodes of the LMO + LZC | Li-In and LMO + LTC | Li-In cells. The samples were discharged to 2.32 V and 2.02 V *vs.* Li/Li^+, respectively, prior to analysis. For the LMO + LZC | Li-In cell, high-angle annular dark-field (HAADF) images show that LMO maintains a granular morphology after deep discharge (Figure 5(a)). A higher-magnification image reveals that the LMO particle is divided into two regions by a grain boundary (Fig. 5(b)). Although the atomic arrangements in these two regions appear similar, lattice spacing measurements and fast Fourier transform (FFT) analysis based on the corresponding simulated images (Fig. 5(h), 5(i)) indicate that the upper-left region corresponds to the spinel LMO phase, whereas the lower-right region corresponds to the rock-salt $Li_2Mn_2O_4$ phase (Fig. 5(b–d) and Fig. S17). The formation of rock-salt $Li_2Mn_2O_4$ during deep discharge is induced by Jahn-Teller distortion and severely impedes Li^+ diffusion, thereby deteriorating the long-term cycling performance of the battery (Fig. 5(g–i)).

To further confirm the phase assignment of these two structurally similar regions, geometric phase analysis (GPA) was conducted on the atomic-resolution images (Fig. 5(c–f)). The results reveal a compressive strain of approximately −1% along the x-direction near the grain boundary, while the strain along the y-direction is negligible (Fig. 5(e), 5(f) and Fig. S18). This strain originates primarily from lattice mismatch between the (0 2 2) plane of spinel LMO and the (0 2 0) plane of rock-salt $Li_2Mn_2O_4$ (Fig. 5(e)). High-resolution EDS mapping detects only Mn and O signals within the LMO particles, with almost no detectable Zr signal (Fig. 5(j), 5(k)). Notably, during STEM sample preparation, pure water was used to dissolve and remove LZC and LTC to minimize catholyte-related signal interference. These results confirm that, for ASSLBs employing catholyte-based composite cathodes, the performance degradation below 2.92 V *vs.* Li/Li^+ is primarily caused by Jahn-Teller distortion–induced phase transformation.

In contrast, the LMO + LTC | Li-In cell exhibits markedly different structural features after deep discharge. HAADF images show that LMO particles remain granular (Fig. 5(l)).

However, unlike the well-ordered atomic arrangement observed in the LMO + LZC | Li-In cell (Fig. 5(b)), the atomic-resolution image of LMO in the LMO + LTC | Li-In cell lacks large regions of long-range order (Fig. 5(m)). Local FFT analysis fails to conclusively assign the structure to either spinel LMO or rock-salt $Li_2Mn_2O_4$ (Fig. 5(m)). Moreover, the presence of extensive lattice distortion is evidenced by GPA results, which reveal pronounced strain fluctuations of approximately ±10% along both the x and y directions (Fig. 5(n–q) and Fig. S19). These significant structural deviations suggest that LMO undergoes additional electrochemical reactions in the presence of LTC, leading to the formation of new phases. High-resolution EDS mapping further confirms the presence of substantial Ti signals within the LMO particles, in addition to Mn and O signals (Fig. 5(u), 5(v)). Previous researches have demonstrated that elements such as Al, Co, Cu, Ti, and Gd have been doped into the 16*c* sites of the LMO lattice, reducing crystallinity and homogenizing the local electronic environment of Mn^{3+}, thereby mitigating Jahn-Teller distortion [19, 21]. Based on these observations, we proposed that during deep discharge in the voltage range of 2.92–2.02 V *vs.* Li/Li^+, Ti atoms originating from the LTC cathode are electrochemically inserted into the 16*c* sites of the LMO lattice, forming a Ti-doped spinel phase denoted as $Li_2Mn_2Ti_xO_4$ (Fig. 5(r)).

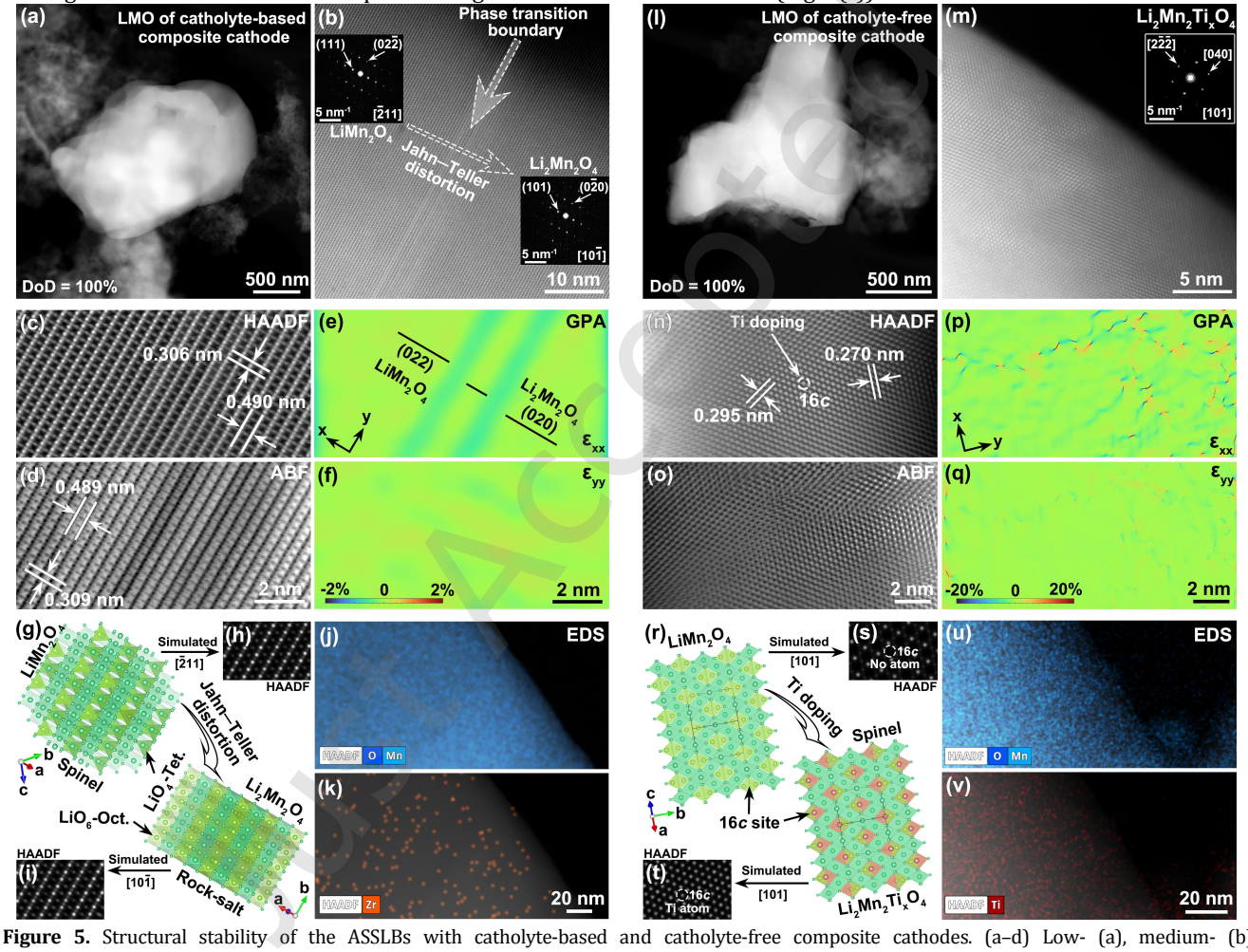

Figure 5. Structural stability of the ASSLBs with catholyte-based and catholyte-free composite cathodes. (a–d) Low- (a), medium- (b), high-magnification (c) HAADF and ABF (d) images of LMO in LMO + LZC | Li-In cell after cycled. (e, f) Strain maps obtained by performing GPA on the image in (c). (g) Atomic model of spinel LMO along the [$\bar{2}$11] zone axis and rock-salt $Li_2Mn_2O_4$ along the [10$\bar{1}$] zone axis. (h, i) Simulated HAADF images of spinel LMO (h) and rock-salt $Li_2Mn_2O_4$ (i). (j, k) EDS mapping results of LMO in LMO + LZC | Li-In cell after cycled. (l–o) Low- (l), medium- (m), high-magnification (n) HAADF and ABF (o) images of LMO in LMO + LTC | Li-In cell after cycled. (p, q) Strain maps obtained by performing GPA on the image in (n). (r) Atomic model of spinel LMO and $Li_2Mn_2Ti_xO_4$ along the [101] zone axis. (s, t) Simulated HAADF images of spinel LMO (s) and $Li_2Mn_2Ti_xO_4$ (t). (u, v) EDS mapping results of LMO in LMO + LTC | Li-In cell after cycled.

To visually corroborate the effect of Ti insertion, HAADF images were simulated using corresponding crystal structure models [50]. The simulated image of pristine spinel LMO viewed along the [101] zone axis shows no atomic contrast at the 16*c* sites, which appear as dark regions (Fig. 5(s)). In contrast, the simulated spinel $Li_2Mn_2Ti_xO_4$ structure exhibits distinct bright contrast at the 16*c* sites due to the presence of Ti atoms (Fig. 5(t)). Importantly, the experimentally observed atomic images that could not be indexed as either spinel LMO or rock-salt $Li_2Mn_2O_4$ (Fig. 5(m–o)) closely match the simulated $Li_2Mn_2Ti_xO_4$ image, and the corresponding FFT patterns are consistent with the [101] zone axis of spinel $Li_2Mn_2Ti_xO_4$ (Fig. 5(m)). These results confirm that

the LMO + LTC | Li-In cell forms a Ti-doped spinel $Li_2Mn_2Ti_xO_4$ phase after deep discharge. Further evidence and inferences concerning the $Li_2Mn_2Ti_xO_4$ phase were provided in the Experimental section (Figs. S20–S25). This structural evolution is also consistent with the emergence of new characteristic peaks in the dQ/dV curves after the first charge–discharge cycle (Fig. 4(e)). Although the precise Ti content cannot be quantified in this study, the consumption of Ti during cycling likely contributes to the gradual attenuation of the LTC-related redox peaks in the dQ/dV curves, which may affect the long-term cycling stability of the LTC cathode. Overall, these results demonstrate that Ti insertion from LTC into the LMO lattice reduces the crystallinity of LMO and suppresses Jahn-Teller distortion, thereby enabling significantly improved long-term cycling performance under deep charge-discharge conditions.

3 Conclusions

In summary, we present a catholyte-free composite cathode by integrating LMO with the redox-active halide LTC, replacing the conventional inert catholyte in ASSLBs. during deep charge–discharge cycling, Ti originating from LTC are electrochemically incorporated into the LMO lattice, forming a Ti-doped spinel phase, $Li_2Mn_2Ti_xO_4$. This lattice modification disrupts the long-range ordering of Mn^{3+} ions and effectively suppresses Jahn-Teller distortion, which is a major degradation pathway for manganese-based spinel cathodes under low-voltage operation. As a result, the catholyte-free composite cathode delivers a substantially enhanced discharge specific capacity of 316.3 mAh g^{-1} and exhibits markedly improved cycling stability, retaining 97.5 mAh g^{-1} after 500 cycles under deep discharge conditions. The ASSLPB with catholyte-free composite cathode enables a gravimetric energy density of up to 588.8 Wh kg^{-1}, representing an approximately 2.3-fold increase compared with conventional catholyte-based composite cathodes. This approach demonstrates a scalable, cost-effective solution for enhancing energy density and stability in manganese-based spinel oxide cathodes for ASSLBs.

Acknowledgements

The authors acknowledge the National Natural Science Foundation of China (52502262, 22479068, 52402311, 22405109, 22579074), the Key Research and Development Program of Gansu Province - Industrial Project under Grant (25YFGA001), the Natural Science Foundation of Gansu Province (24JRRA470, 24JRRA472, 26JRRA689), the Youth Science and Technology Foundation of Sichuan Province (2025ZNSFSC1376), the Innovation Fund of Education Department of Gansu Province (2026A-168).

Declaration of conflicting interests

The authors declare no conflicting interests regarding the content of this article.

Data availability

All data needed to support the conclusions in the paper are presented in the manuscript and/or the Supplementary Materials. Additional data related to this paper may be requested from the corresponding author upon request.

Electronic Supplementary Material: Supplementary material (experimental section, STEM images, Nyquist plot, dQ/dV curves, Estimation of the gravimetric/volumetric energy density) is available in the online version of this article at https://doi.org/10.26599/NRE.2026.9120273.

References

[1] J. Fu, C. Wang, S. Wang, J. W. Reid, J. Liang, J. Luo, J. T. Kim, Y. Zhao, X. Yang, F. Zhao, W. Li, B. Fu, X. Lin, Y. Hu, H. Su, X. Hao, Y. Gao, S. Zhang, Z. Wang, J. Liu, H. Abdolvand, T.-K. Sham, Y. Mo, X. Sun, A cost-effective all-in-one halide material for all-solid-state batteries, *Nature* **2025**, *643*, 111.

[2] F. Zhao, S. Zhang, S. Wang, J. W. Reid, W. Xia, J. Liu, G. King, J. A. Kaduk, J. Liang, J. Luo, Y. Gao, F. Yang, Y. Zhao, W. Li, S. H. Alahakoon, J. Guo, Y. Huang, T.-K. Sham, Y. Mo, X. Sun, Anion sublattice design enables superionic conductivity in crystalline oxyhalides, *Science* **2025**, *390*, 199.

[3] J. Pei, X. Bai, P. Xue, L. Ma, R. Long, Z. Liu, W. Liu, All-solid-state battery safety in abnormal thermal situations: Crack propagation and lithium dendrite growth, *Nano Res. Energy* **2025**, *4*, e9120155.

[4] J. Peng, Y. Li, X. Li, J. Huang, B. Zou, F. Zheng, Q. Pan, H. Wang, Q. Li, S. Hu, Surface anchored Al-doped $Li_7La_3Zr_2O_{12}$ induced order-disorder arrangement for high-performance Li-rich layered cathodes, *Nano Res. Energy* **2026**, *5*, e9120209.

[5] Z. Zeng, J. Cheng, Y. Li, H. Zhang, D. Li, H. Liu, F. Ji, Q. Sun, L. Ci, Composite cathode for all-solid-state lithium batteries: Progress and perspective, *Mater. Today Phys.* **2023**, *32*, 101009.

[6] J. Xu, W.-L. Wong, H. Du, Y. Kang, Y. Zhao, B. Lan, Z. Guo, M.-M. Titirici, F. Kang, B. Li, Upcycling the cathodes of spent lithium ion batteries into high-performance cathodes, *Nano Res. Energy* **2025**, *4*, e9120174.

[7] X. Li, Z. Dai, Z. Xu, Q. Li, H. Liu, K. Lv, A. Bayaguud, High-voltage and high-capacity oxide cathode materials in sulfide-based all–solid–state lithium batteries, *J. Energy Storage* **2025**, *121*, 116504.

[8] C. Wang, J. Liang, Y. Zhao, M. Zheng, X. Li, X. Sun, All-solid-state lithium batteries enabled by sulfide electrolytes: from fundamental research to practical engineering design, *Energy Environ. Sci.* **2021**, *14*, 2577.

[9] S. Randau, D. A. Weber, O. Kötz, R. Koerver, P. Braun, A. Weber, E. Ivers-Tiffée, T. Adermann, J. Kulisch, W. G. Zeier, F. H. Richter, J. Janek, Benchmarking the performance of all-solid-state lithium batteries, *Nat. Energy* **2020**, *5*, 259.

[10] C. Wang, S. Wang, X. Liu, Y. Wu, R. Yu, H. Duan, J. T. Kim, H. Huang, J. Wang, Y. Mo, X. Sun, New insights into aliovalent

substituted halide solid electrolytes for cobalt-free all-solid state batteries, *Energy Environ. Sci.* **2023**, *16*, 5136.

[11] L. Zhou, T.-T. Zuo, C. Y. Kwok, S. Y. Kim, A. Assoud, Q. Zhang, J. Janek, L. F. Nazar, High areal capacity, long cycle life 4 V ceramic all-solid-state Li-ion batteries enabled by chloride solid electrolytes, *Nat. Energy* **2022**, *7*, 83.

[12] T. A. Hendriks, M. A. Lange, E. M. Kiens, C. Baeumer, W. G. Zeier, Balancing partial ionic and electronic transport for optimized cathode utilization of high‐voltage $LiMn_2O_4$/Li_3InCl_6 solid‐state batteries, *Batteries Supercaps* **2023**, *6*, e202200544.

[13] Y. Dou, S. Zhou, J. I. G. Dawkins, K. Zaghib, K. Amine, G. L. Xu, S. Deng, Manganese‐based spinel cathodes: A promising frontier for solid‐state lithium‐ion batteries, *Adv. Mater.* **2025**, *38*, e14126.

[14] K. Xia, Z. Yao, Z. Liu, S. Luo, H. Xie, X. Li, X. Yao, G. Liang, P. Zhang, Hierarchical ionic networks in polymer electrolyte boost high-voltage solid-state Li batteries with stable interfaces and long cycling, *Nano Res. Energy* **2026**, *5*, e9120181.

[15] K. Wang, Q. Ren, Z. Gu, C. Duan, J. Wang, F. Zhu, Y. Fu, J. Hao, J. Zhu, L. He, C.-W. Wang, Y. Lu, J. Ma, C. Ma, A cost-effective and humidity-tolerant chloride solid electrolyte for lithium batteries, *Nat. Commun.* **2021**, *12*, 4410.

[16] J. Xu, X. Ji, J. Zhang, C. Yang, P. Wang, S. Liu, K. Ludwig, F. Chen, P. Kofinas, C. Wang, Aqueous electrolyte design for super-stable 2.5 V $LiMn_2O_4$ || $Li_4Ti_5O_{12}$ pouch cells, *Nat. Energy* **2022**, *7*, 186.

[17] Q. Wang, L. Liu, H. Li, G. Yang, A. N. Alodhayb, J. Ma, Recent advance in coating strategies for lithium-rich manganese-based cathode materials, *J. Mater. Sci. Technol.* **2025**, *207*, 274.

[18] H. Shang, Q. He, L. Yan, E. Xiaoye, J. Xu, Y. Mu, Z. Y. Li, K. Sun, D. Chen, B. Li, H. Shan, H. Xie, Elucidating the role of intralayer cation ordering and disordering in $Li_{0.6}[Li_{0.2}Mn_{0.8}]O_2$ cathode materials, *Carbon Energy* **2025**, *7*, e70072.

[19] S. Zhou, J. Liao, C. Yu, P. Dai, T. Gao, T. Hou, G. Cao, S. Zhao, Generality rules and synergistic effect of mitigating the Jahn–Teller effect by multisites compositionally complex doping, *ACS Nano* **2024**, *18*, 35356.

[20] S. Yang, P. Yan, W. Bao, H. Zhu, X. Cai, L. Zhao, Y. Zhang, W. Lin, Y. Deng, Y. Wu, J. Xie, Surface magnesium substitution at spinel lithium manganate 8a tetrahedral sites for suppressed manganese dissolution and enhanced cycle stability, *ACS Energy Lett.* **2023**, *8*, 4278.

[21] W. Zeng, F. Xia, J. Wang, J. Yang, H. Peng, W. Shu, Q. Li, H. Wang, G. Wang, S. Mu, J. Wu, Entropy-increased $LiMn_2O_4$-based positive electrodes for fast-charging lithium metal batteries, *Nat. Commun.* **2024**, *15*, 7371.

[22] Y. Wang, S. Liu, X. Guo, B. Wang, Q. Zhang, Y. Li, Y. Wang, G. Wang, L. Gu, H. Yu, Elements gradient doping in Mn-based Li-rich layered oxides for long-life lithium-ion batteries, *J. Mater. Sci. Technol.* **2025**, *207*, 266.

[23] T. Chen, J. Yang, L. Barroso-Luque, G. Ceder, Removing the two-phase transition in spinel $LiMn_2O_4$ through cation disorder, *ACS Energy Lett.* **2022**, *8*, 314.

[24] A. Dutta, S. Beniwal, A. Van Der Est, W. Song, S. Yu, M. Johnson, P. Xiao, J. R. Dahn, C. Yang, Evolution of spinel $LiMn_2O_4$ single crystal morphology induced by the Li_2MnO_3 phase during sintering, *ACS Energy Lett.* **2024**, *9*, 888.

[25] W. Ou, S. D. Marks, R. F. de Menezes, R. He, Z. Zhang, C. Sindt, J. Thurston, C. Jaye, B. Cowie, L. Thomsen, Z. Zhuo, J. Guo, W. Yang, Z. Dong, R. Tenent, K. G. Sprenger, M. F. Toney, Unveiling the mechanism of Mn dissolution through a dynamic cathode‐electrolyte interphase on $LiMn_2O_4$, *Adv. Energy Mater.* **2025**, *15*, 2404652.

[26] L. Hu, J. Wang, K. Wang, Z. Gu, Z. Xi, H. Li, F. Chen, Y. Wang, Z. Li, C. Ma, A cost-effective, ionically conductive and compressible oxychloride solid-state electrolyte for stable all-solid-state lithium-based batteries, *Nat. Commun.* **2023**, *14*, 3807.

[27] K. Wang, Z. Gu, Z. Xi, L. Hu, C. Ma, Li_3TiCl_6 as ionic conductive and compressible positive electrode active material for all-solid-state lithium-based batteries, *Nat. Commun.* **2023**, *14*, 1396.

[28] X. Zhou, M. Jiang, Y. Duan, Z. Jia, C. Yuan, K. Feng, Q. Fu, L. Zhang, X. Yang, X. Li, Multi‐electron transfer halide cathode materials based on intercalation‐conversion reaction towards all‐solid‐state lithium batteries, *Angew. Chem. Int. Edit.* **2024**, *64*, e202416635.

[29] D. Peng, R. Li, K. Xu, R. Si, Z. Zhang, Y.-S. Hu, A low-strain lithium cathode material $Li_{2-2x}Fe_{1+x}Cl_4$ for halide-based all-solid-state batteries, *ACS Energy Lett.* **2025**, *10*, 1421.

[30] Z. Song, Y. Dai, T. Wang, Q. Yu, X. Ye, L. Wang, Y. Zhang, S. Wang, W. Luo, An active halide catholyte boosts the extra capacity for all‐solid‐state batteries, *Adv. Mater.* **2024**, *36*, 2405277.

[31] G. Zhang, Z. Liu, Y. Ma, J. Pepas, J. Bai, H. Zhong, Y. Tang, H. Chen, $Li_{2.9}Fe_{0.9}Zr_{0.1}Cl_6$ as redox-active catholyte for solid-state Li-ion batteries, *Chem. Mater.* **2024**, *36*, 10104.

[32] B. H. Toby, R. B. Von Dreele, GSAS-II: the genesis of a modern open-source all purpose crystallography software package, *J. Appl. Crystallogr.* **2013**, *46*, 544.

[33] R. B. Von Dreele, Small-angle scattering data analysis in GSAS-II, *J. Appl. Crystallogr.* **2014**, *47*, 1784.

[34] H. Zhou, Z. Gu, M. Li, M. Fan, Z. Zhao, S. Fu, K. Wang, SEM characterization technique for air-sensitive all-solid-state lithium battery materials, *Ultramicroscopy* **2025**, *276*, 114194.

[35] Q. Xia, X. Lei, F. Yue, W. Liu, C. Xu, J. Xu, M. Yang, X. Huang, D. Su, H. Xia, Unraveling the $LiMn_2O_4$/LiPON interface degradation in all-solid-state thin-film lithium batteries, *Nano Lett.* **2025**, *25*, 7892.

[36] D. Xu, M. Jin, Z. Su, R. Liu, M. Xiang, W. Fang, L. He, R. Wu, Y. Guo, Facile synthesis of inorganic $Li_2B_{12}H_{12}$/LiI solid electrolytes for high‐voltage all‐solid‐state lithium batteries, *Adv. Sci.* **2025**, *12*, e10193.

[37] K. Ghosh, M. Wasim Raja, Facile Li-ion transport in microstructurally engineered hybrid LLZO electrolyte for application in pseudo-solid state lithium metal batteries, *Chem. Eng. J.* **2024**, *480*, 148200.

[38] P. Gami, M. Badole, H. N. Vasavan, A. K. Das, S. Saxena, S. Kumar, Y-doped $LiZr_2(PO_4)_3$ in a PVDF-HFP composite electrolyte for solid-state Li-metal batteries, *ACS Appl. Eng. Mater.* **2024**, *2*, 1278.

[39] K. Ghosh, M. Wasim Raja, Engineered $Li_7La_3Zr_2O_{12}$ (LLZO) for pseudo-solid-state lithium metal batteries (SSLMBs): Tailor-made synthesis, evolution of the microstructure, suppression of dendritic growth, and enhanced electrochemical performance, *ACS Appl. Energy Mater.* **2023**, *6*, 4035.

[40] C. Wang, G. Bai, X. Liu, Y. Li, Favorable electrochemical performance of $LiMn_2O_4$/$LiFePO_4$ composite electrodes attributed to composite solid electrolytes for all-solid-state lithium batteries, *Langmuir* **2021**, *37*, 2349.

[41] J. Auvergniot, A. Cassel, J.-B. Ledeuil, V. Viallet, V. Seznec, R.

Dedryvère, Interface stability of argyrodite Li_6PS_5Cl toward $LiCoO_2$, $LiNi_{1/3}Co_{1/3}Mn_{1/3}O_2$, and $LiMn_2O_4$ in bulk all-solid-state batteries, *Chem. Mater.* **2017**, *29*, 3883.

[42] M. Hara, H. Nakano, K. Dokko, S. Okuda, A. Kaeriyama, K. Kanamura, Fabrication of all solid-state lithium-ion batteries with three-dimensionally ordered composite electrode consisting of $Li_{0.35}La_{0.55}TiO_3$ and $LiMn_2O_4$, *Journal of Power Sources* **2009**, *189*, 485.

[43] J. Johnson, S. R. Sasirajan Littleflower, K. Vediappan, H. Annal Therese, Alleviating Mn ion dissolution in $LiMn_2O_4$ by activation of TiO_2 Lewis acid sites in electrospun PVA/TiO_2 quasi-solid polymer electrolyte, *Nano Lett.* **2025**, *25*, 5983.

[44] E. Kim, J. Lee, J. Park, H. Kim, K. W. Nam, Conductive MOF-derived coating for suppressing the Mn dissolution in $LiMn_2O_4$ toward long-life lithium-ion batteries, *Nano Lett.* **2025**, *25*, 619.

[45] Y. Lu, C.-Z. Zhao, J.-Q. Huang, Q. Zhang, The timescale identification decoupling complicated kinetic processes in lithium batteries, *Joule* **2022**, *6*, 1172.

[46] T. H. Wan, M. Saccoccio, C. Chen, F. Ciucci, Influence of the discretization methods on the distribution of relaxation times deconvolution: implementing radial basis functions with DRTtools, *Electrochim. Acta* **2015**, *184*, 483.

[47] M. Dixit, A. Parejiya, R. Essehli, N. Muralidharan, S. U. Haq, R. Amin, I. Belharouak, SolidPAC is an interactive battery-on-demand energy density estimator for solid-state batteries, *Cell Rep. Phys. Sci.* **2022**, *3*, 100756.

[48] S. Sun, R. Zhang, Z. Gu, X. Fang, T. Ma, H. Li, Z. Lin, H. Yi, X. Zhang, L. Wu, K. Sun, D. Liu, Y. Wu, H. Ma, Y. Fu, K. Wang, D. He, Interfacial stabilization mechanism of zirconium‐based halide and Li–In alloy anode in all‐solid‐state lithium batteries, *Adv. Energy Mater.* **2025**, *37*, 2500390.

[49] M. Burton, S. Narayanan, B. Jagger, L. F. Olbrich, S. Dhir, M. Shibata, M. J. Lain, R. Astbury, N. Butcher, M. Copley, T. Kotaka, Y. Aihara, M. Pasta, Techno-economic assessment of thin lithium metal anodes for solid-state batteries, *Nat. Energy* **2024**, *10*, 135.

[50] J. Barthel, Dr. Probe: A software for high-resolution STEM image simulation, *Ultramicroscopy* **2018**, *193*, 1.

Zheyuan Lin received his BS degree (2025) in Lanzhou University. He is currently a master's student in the research group of Prof. Kai Wang in the School of Materials & Energy, Lanzhou University. His research interests focus on the development of new halide cathode materials.

Zhenqi Gu received her BS degree (2018) in Southeast University, and PhD degree (2023) in University of Science and Technology of China. She is currently an assistant professor at School of Materials Science and Engineering, Xihua University. Her research primarily focuses on the study and optimization of solid-state electrolytes and solid electrolyte/electrode interfaces, including elucidating the effects of defects in solid-state electrolyte materials on their properties, improving physical contact between solid-state electrolytes and electrode particles, and developing novel electrode and solid electrolyte materials for all-solid-state lithium batteries.

Kai Wang received his BS degree (2016) and MS degree (2019) in Tianjin University of Technology, and PhD degree (2022) in University of Science and Technology of China. He is currently a professor at School of Materials & Energy, Lanzhou University. His research focuses on the development of novel electrode and electrolyte materials for all- solid- state lithium batteries, and the investigation of electrochemical energy storage mechanisms using advanced electron microscopy techniques.

Deyan He received his bachelor's degree (1982) and MS degree (1985) in Solid State Physics from Lanzhou University in China, and PhD degree (1995) in Electronic Chemistry from Tokyo Institute of Technology in Japan. He is currently a professor at School of Materials & Energy, Lanzhou University. His current research involves development and application of Advanced Electronic and Energy Materials, mainly including silicon-based thin films and metal oxide-based materials for solar cells, lithium ion batteries, and other devices.

Electronic Supplementary Material

Catholyte-free composite cathodes to improve the energy density of low-cost $LiMn_2O_4$-based all-solid-state lithium batteries

Zheyuan Lin[1,§], Zhenqi Gu[1,2,§], Rongcheng Zhang[1], Shiqing Sun[1], Tian Ma[1], Haosen Li[1], Yibo Niu[1], Yuanyuan Nie[1], Xianyu Liu[3], Ying Wu[1], Hongyun Ma[1], Yujun Fu[1], Junshuai Li[1], Kai Wang[1] (✉), and Deyan He[1] (✉)

[1] *School of Materials & Energy, Lanzhou University, Lanzhou 730000, China*
[2] *School of Materials Science and Engineering, Xihua University, Chengdun 610039, China*
[3] *Bailie School of Petroleum Engineering, Lanzhou City University, Lanzhou 730070, China*
[§] *These authors contributed equally to this work.*

Supporting information to https://doi.org/10.26599/NRE.2026.9120273

Address correspondence to kai Wang, kwang@lzu.edu.cn; Deyan He, hedy@lzu.edu.cn

Experimental Section

Structural characterization: The synthesis conditions of LTC and LZC were consistent with those previously reported. XRD tests were conducted using a copper target diffractometer (Malvern Panalytical, 40 kV and 40 mA), with XRD refinement performed using the GSAS II software. Except for the scan speed of 5° min^{-1} for the refined data, other scans were conducted at 10° min^{-1}. Surface morphology and composition analysis of the samples were performed using a SEM (HITACHI SU8600), with secondary electron images collected at 5 kV and EDS data collected at 10 kV. Notably, during the XRD and SEM tests, Kapton film and an argon-protected transfer box were used to prevent the samples from being exposed to air. High-resolution atomic-scale structure analysis was performed using a STEM (Titan Cubed Themis G2 300) with an acceleration voltage of 300 kV. HAADF imaging simulations were conducted using Dr. Probe software, with the simulated imaging conditions closely matching the actual experimental conditions. The relevant parameter information for the DRT fitting, including the following: the method of discretization was set to gaussian; the regularization derivative was set to fitting w/o inductance; the regularization parameter was set to 1st-order; the RBF shape control was set to full widths at half maximum (FWHM) coefficient with a value of 0.5; and the analysis was ultimately completed using a simple fitting method.

Electrochemical characterizations: The conventional catholyte-based composite cathode was prepared with LMO, LZC, and C in a mass ratio of 70:27:3, and the catholyte-free composite cathode was prepared with LMO, LTC, and C in a mass ratio of 70:27:3. These mixtures were blended in a vortex mixer (Lichen, LC-Vortex MT) at 1000 rpm for 60 minutes. Approximately 6 mg of conventional catholyte-based composite cathode or catholyte-free composite cathode was evenly sprinkled on the stainless steel electrode placed in a 10 mm diameter PEEK mold, followed by about 10 mg of LZC, which was then pressed under 0.5 tons of pressure for 1 minute. After releasing the pressure, 20 mg of LZC and 30 mg of LPSCl (Ganfeng Lithium Group Co., Ltd.) were evenly sprinkled, and the mixture was pressed again under 3 tons of pressure for 5 minutes. Finally, indium foil (ϕ10, 0.1mm thickness, 99.999%, Qinghe County Aoshuo Metal Material Co., Ltd.) and lithium foil (ϕ10, 0.05 mm thickness, 99.9%, China Energy Lithium Co., Ltd.) were sequentially placed on the LPSCl layer. During the battery cycling on the electrochemical performances (CT3002A, Wuhan Land Electronics Co., Ltd.), an external pressure of approximately 0.5 tons and a constant temperature of 25 °C were maintained (Tianjin Hongnuo Instrument, SPX-250B). In situ electrochemical impedance spectroscopy (EIS) measurements were performed using a electrochemical workstation (Bio-Logic VSP-300) with a bias voltage of 50 mV and a frequency range from 7 MHz to 20 mHz. It should be noted that all battery assemblies were conducted in an argon-protected glove box with water and oxygen content below 0.01 ppm.

Estimation of energy density: SolidPAC software was used to estimate the gravimetric energy density of ASSLPBs based on both conventional catholyte-based composite cathodes and catholyte-free composite cathodes. The design parameters of the ASSLPB, including the active material ratio, catholyte ratio, composite cathode area loading, and current collectors, were shown in Table S3. Parameters such as the molar mass, density, and ionic conductivity of the SSEs reported in other researches were shown in Table S4, where the densities of the materials were calculated based on their theoretical values in their crystallographic files. To improve the accuracy of the estimates, core parameters such as

the open-circuit voltage and discharge capacity at different SOCs were obtained from both the experiments in this paper and values reported in the researches.

Inference of the $Li_2Mn_2Ti_xO_4$ Phase: Structural models of spinel- and rock-salt-phase LMO viewed along different zone axes were constructed, and the corresponding HAADF images and SAED patterns were simulated (Figs. S20 and S21). Consistent with the previous version of the manuscript, the simulated HAADF image of spinel-phase LMO along the [211] zone axis closely resembles that of rock-salt-phase LMO along the [10 1] zone axis. However, their slightly different lattice spacings distinguish the two phases. After cycling the LMO + LTC | Li–In cells, the product exhibited a hexagonal arrangement of Mn atoms in the HAADF image. Among the spinel-phase LMO structures, only that viewed along the [111] zone axis resembles this arrangement (Fig. S20(h)). However, its SAED pattern forms a regular hexagon (R1/R2 = 1, Fig. S20(i)), whereas the cycled product forms an irregular hexagon (R1/R2 = 1.14, Fig. 5(m)). Thus, the product does not exhibit the structural characteristics of spinel-phase LMO viewed along the [111] zone axis. Nor can it be assigned to rock-salt-phase LMO (Fig. S21). The SAED pattern of spinel-phase LMO along the [101] zone axis is relatively similar to that of the cycled product (R1/R2 = 1.16, Fig. S20(f)), but their HAADF images differ clearly (Figs. 5(n) and S20(e)). The cycled product contains an additional small bright spot at the center of the hexagon formed by six small bright spots (Fig. 5(n)), whereas spinel-phase LMO along the [101] zone axis exhibits only a hollow hexagon, with no bright spot at the central 16c site (Fig. S20(e)). EDS mapping further shows a uniform Ti distribution throughout the cycled product (Fig. 5(v)). To test whether Ti occupies the 16c sites during cycling, we placed Ti atoms at these sites and assigned the product to spinel-phase $Li_2Mn_2Ti_xO_4$. We then constructed $Li_2Mn_2Ti_xO_4$ models viewed along different zone axes and simulated the corresponding HAADF images and SAED patterns (Fig. S22). When Ti occupies the 16c sites, the simulated HAADF image of $Li_2Mn_2Ti_xO_4$ along the [101] zone axis agrees with the experimental image (Figs. S22(e) and 5(n)). Its R1/R2 value is 1.14, close to the value of 1.16 for spinel-phase LMO and distinct from those of rock-salt-phase LMO along the [100] and [111] zone axes, which are 1.04 and 1.21 (Fig. S21(c), (l)), respectively. These results essentially exclude a rock-salt structure. Along the [100] and [111] zone axes, the HAADF images of spinel-phase LMO and $Li_2Mn_2Ti_xO_4$ are nearly indistinguishable (Figs. S20(b), (h) and S22(b), (h)); clear differences appear only along the [101] and [211] zone axes (Figs. S20(e), (k) and S22(e), (k)). Identifying the Ti sites therefore requires imaging along specific zone axes. We accordingly oriented uncycled spinel-phase LMO along the [101] zone axis in an aberration-corrected electron microscope and obtained a hollow hexagonal arrangement of six Mn atoms (Fig. S23(a) and (b)). The corresponding FFT pattern yielded R1/R2 = 1.16 (Fig. S23(c)), in excellent agreement with the theoretical value. In contrast, the HAADF and ABF images of spinel-phase $Li_2Mn_2Ti_xO_4$ along the [101] zone axis revealed a Ti atom at the center of the Mn hexagon (Fig. S23(d) and (e)), and its FFT pattern yielded R1/R2 = 1.14 (Fig. S23(f)), close to the value for spinel-phase LMO. The EDS spectrum of uncycled spinel-phase LMO showed only Mn and O signals, with no detectable Ti signal (Fig. S24). After cycling, the spectrum of spinel-phase $Li_2Mn_2Ti_xO_4$ exhibited a distinct Ti signal in addition to the Mn and O signals (Fig. S25). We therefore confirm that low-voltage cycling inserts Ti into the 16c sites of the LMO lattice, forming spinel-phase $Li_2Mn_2Ti_xO_4$.

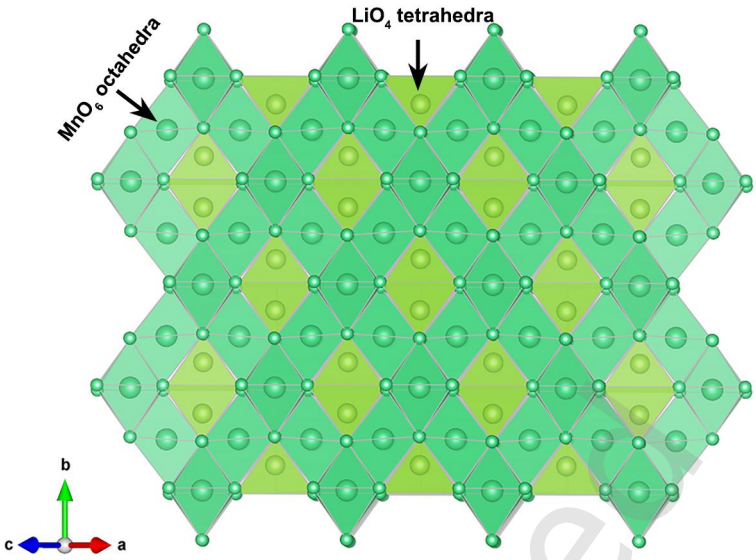

Figure S1. The structural model of spinel LMO.

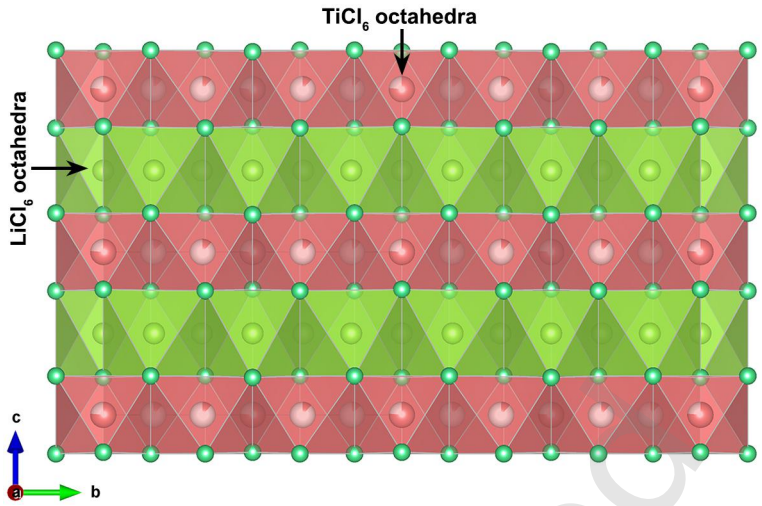

Figure S2. The structural model of layered LTC.

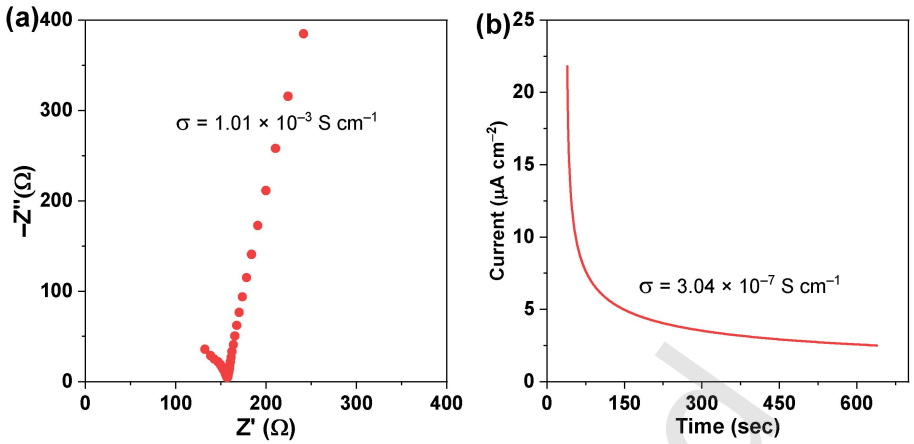

Figure S3. a, b) Nyquist plot and i-t curve of LTC materials at 25 °C, respectively.

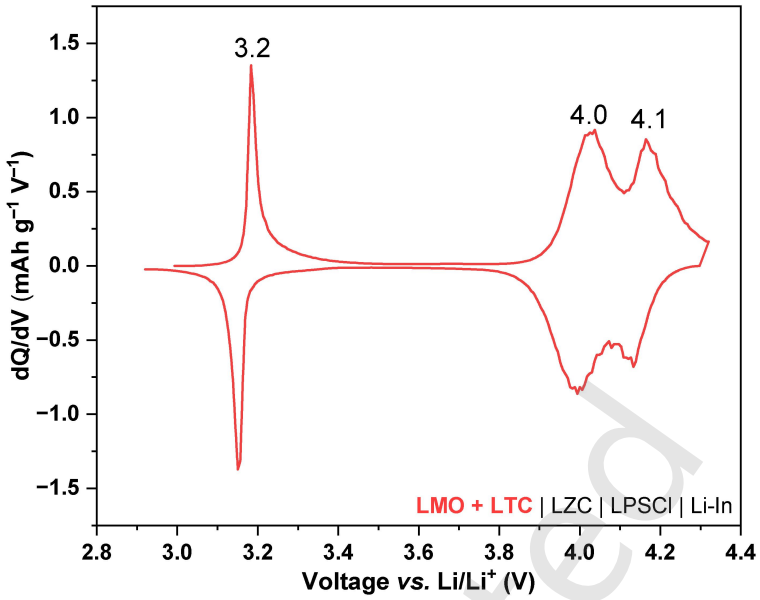

Figure S4. dQ/dV curve of the LMO + LTC | Li-In cell.

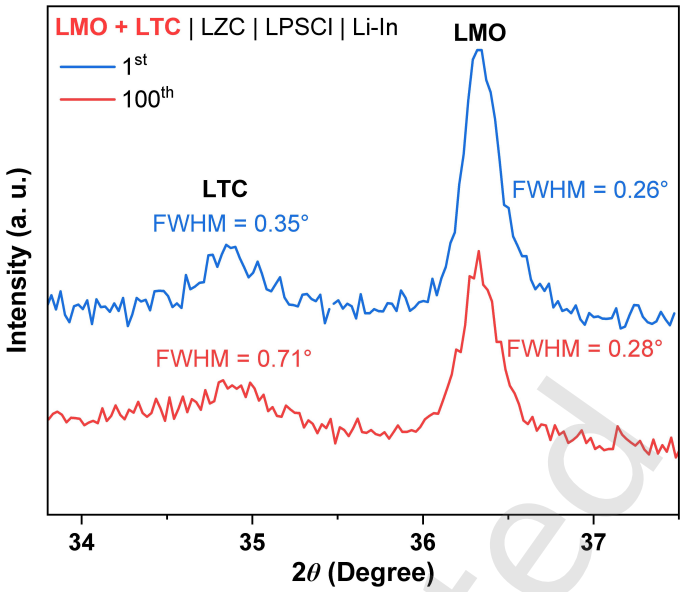

Figure S5. The FWHMs of the (131) and (311) diffraction peaks of LTC and LMO, respectively, during the 1st and 100th cycles of the LMO + LTC | Li-In cells.

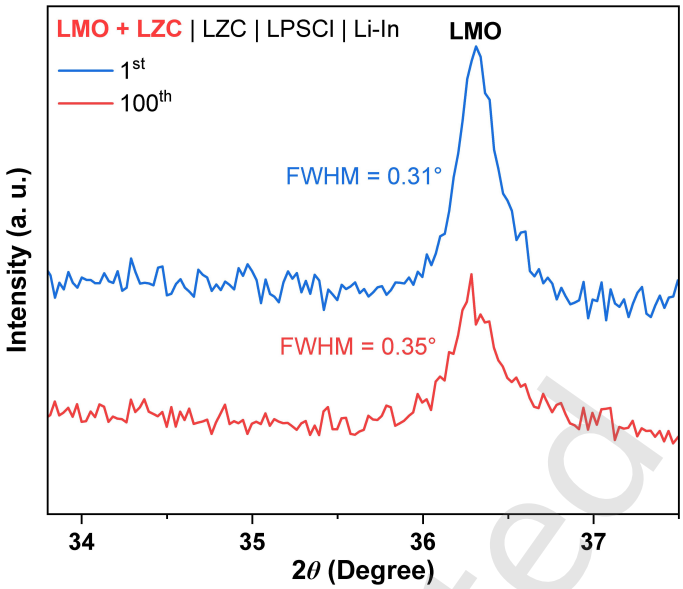

Figure S6. The FWHMs of the (311) diffraction peaks of LMO, during the 1st and 100th cycles of the LMO + LZC | Li-In cells.

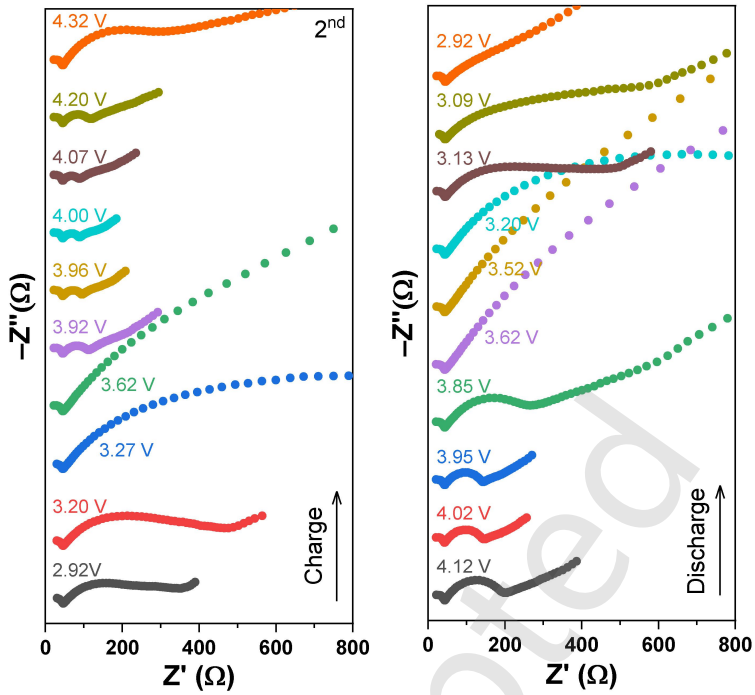

Figure S7. In-situ EIS for the 2nd cycle of LMO + LTC | Li-In cell.

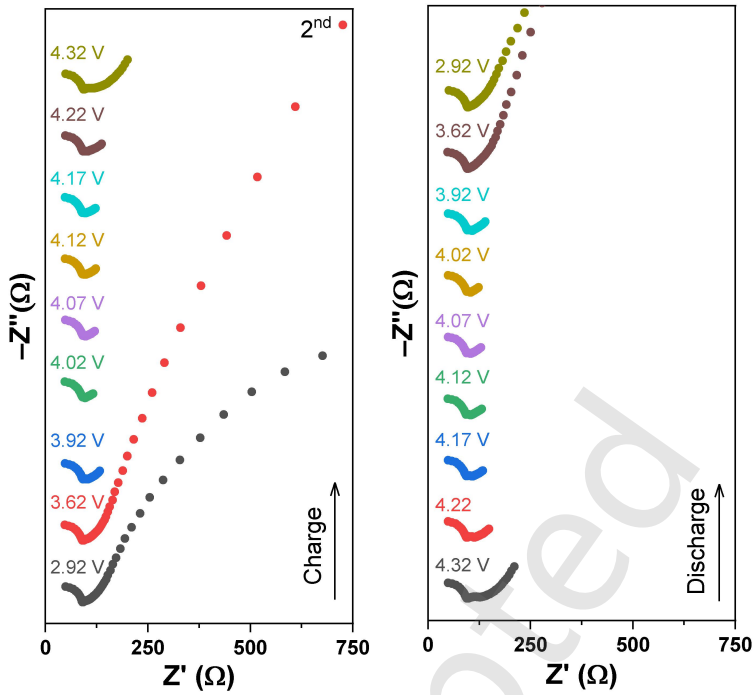

Figure S8. In-situ EIS for the 2nd cycle of LMO + LZC | Li-In cell.

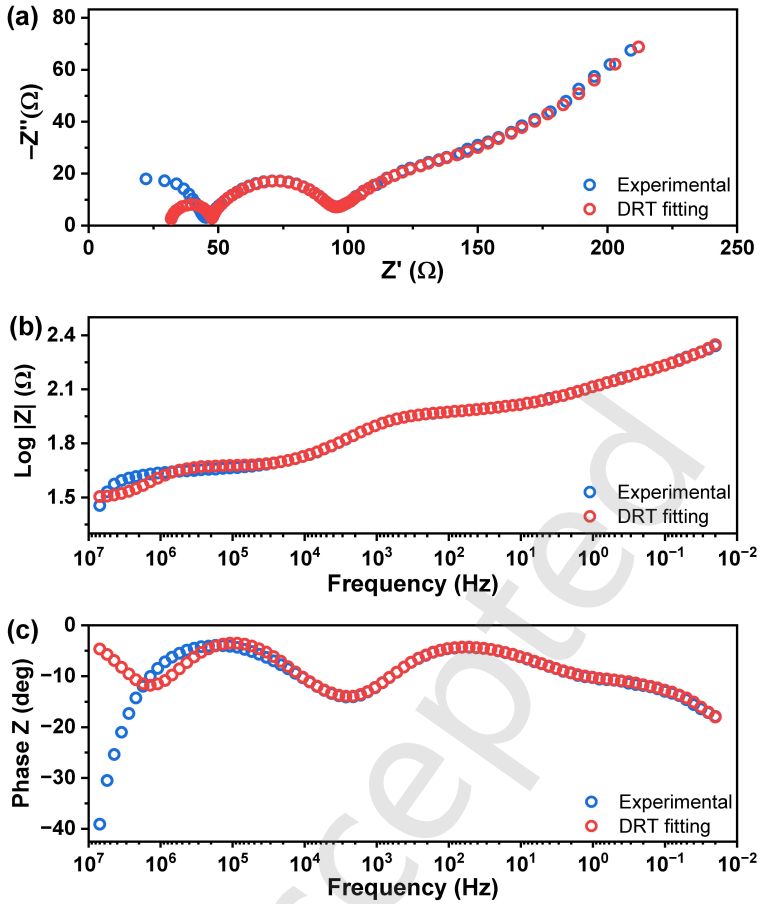

Figure S9. comparative analysis of the experimental data and the DRT fitting data.

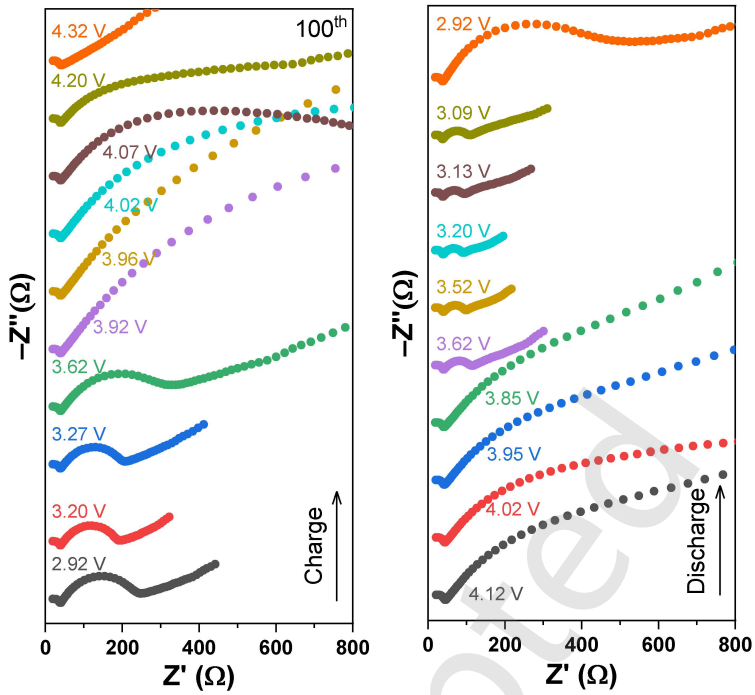

Figure S10. In-situ EIS for the 100th cycle of LMO + LTC | Li-In cell.

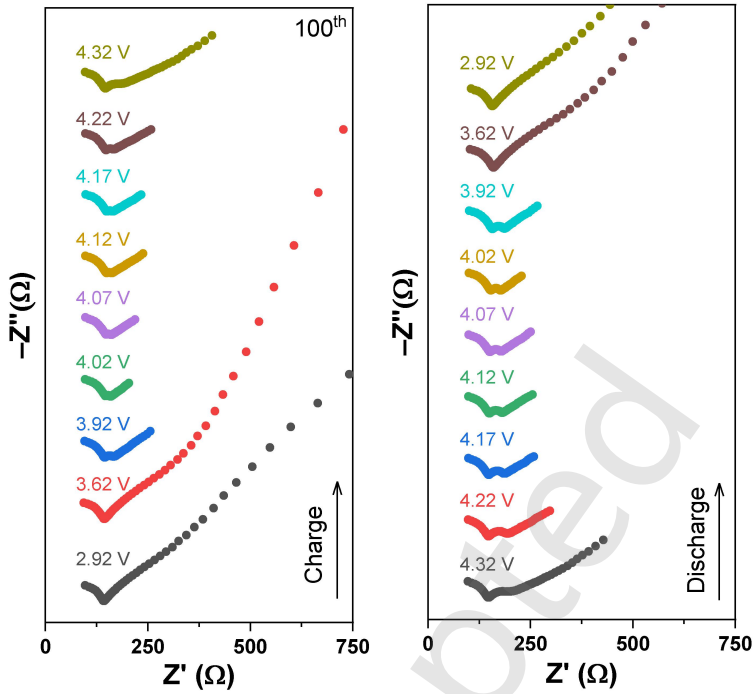

Figure S11. In-situ EIS for the 100th cycle of LMO + LZC | Li-In cell.

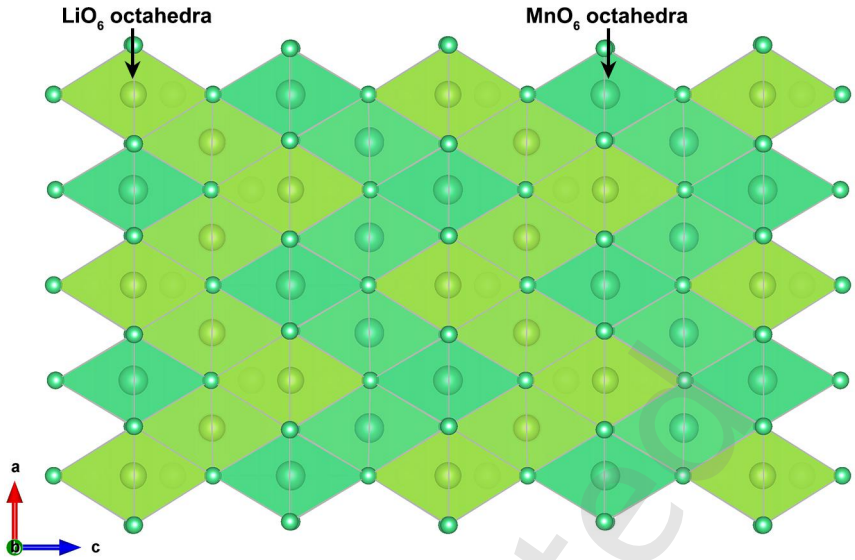

Figure S12. The structural model of rock-salt $Li_2Mn_2O_4$.

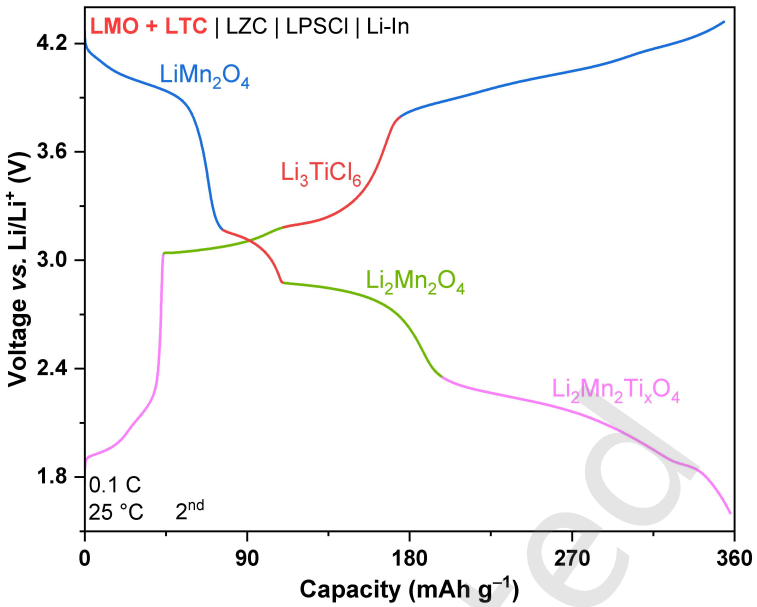

Figure S13. Differentiation of the capacity contributions of LMO and LTC during the charge–discharge process.

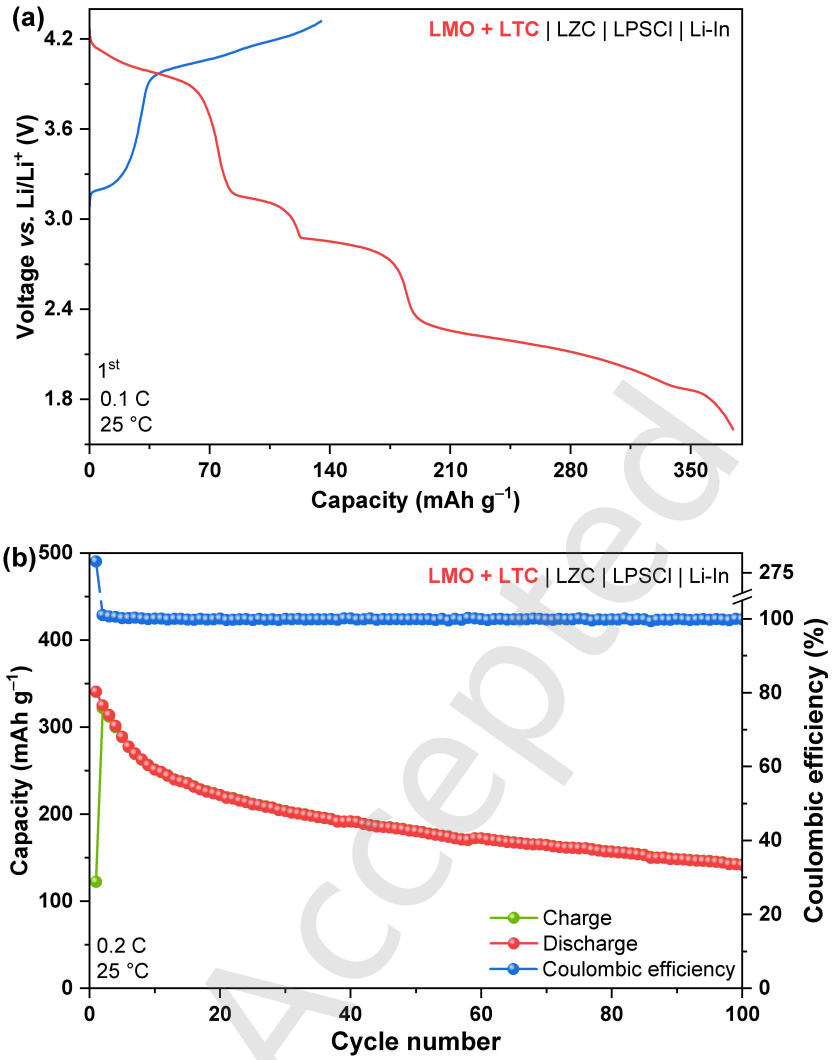

Figure S14. Initial charge/discharge curve (a) and long-term cycling performance (b) of LMO + LTC | Li-In cells at 1.62–4.32 V *vs.* Li/Li^+.

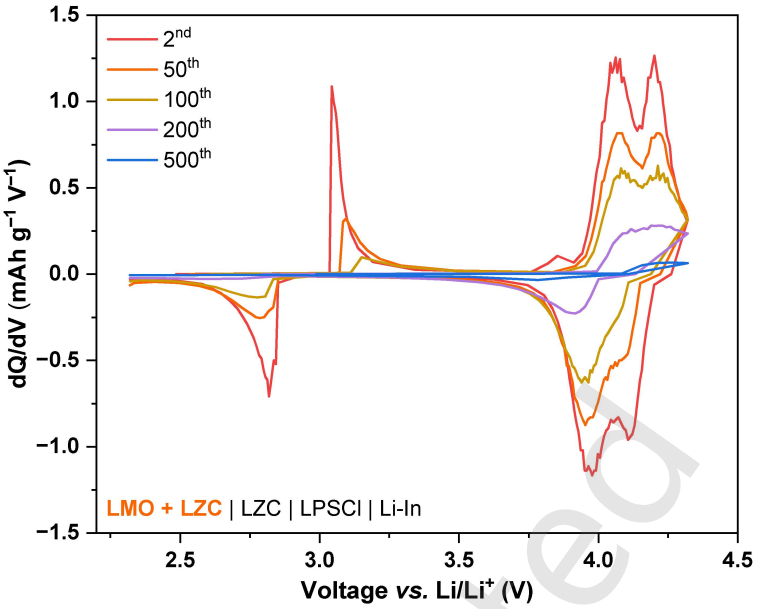

Figure S15. dQ/dV curves of the LMO + LZC | Li-In cell.

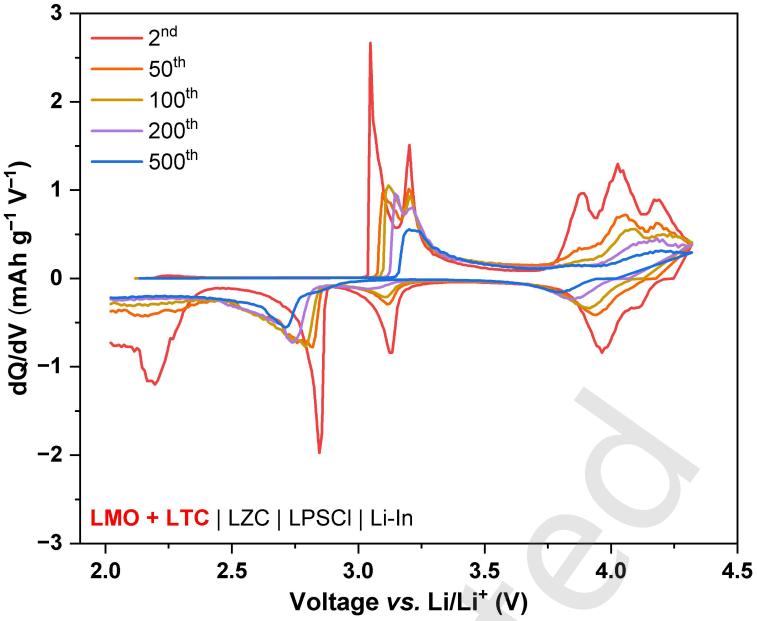

Figure S16. dQ/dV curve of the LMO + LTC | Li-In cell.

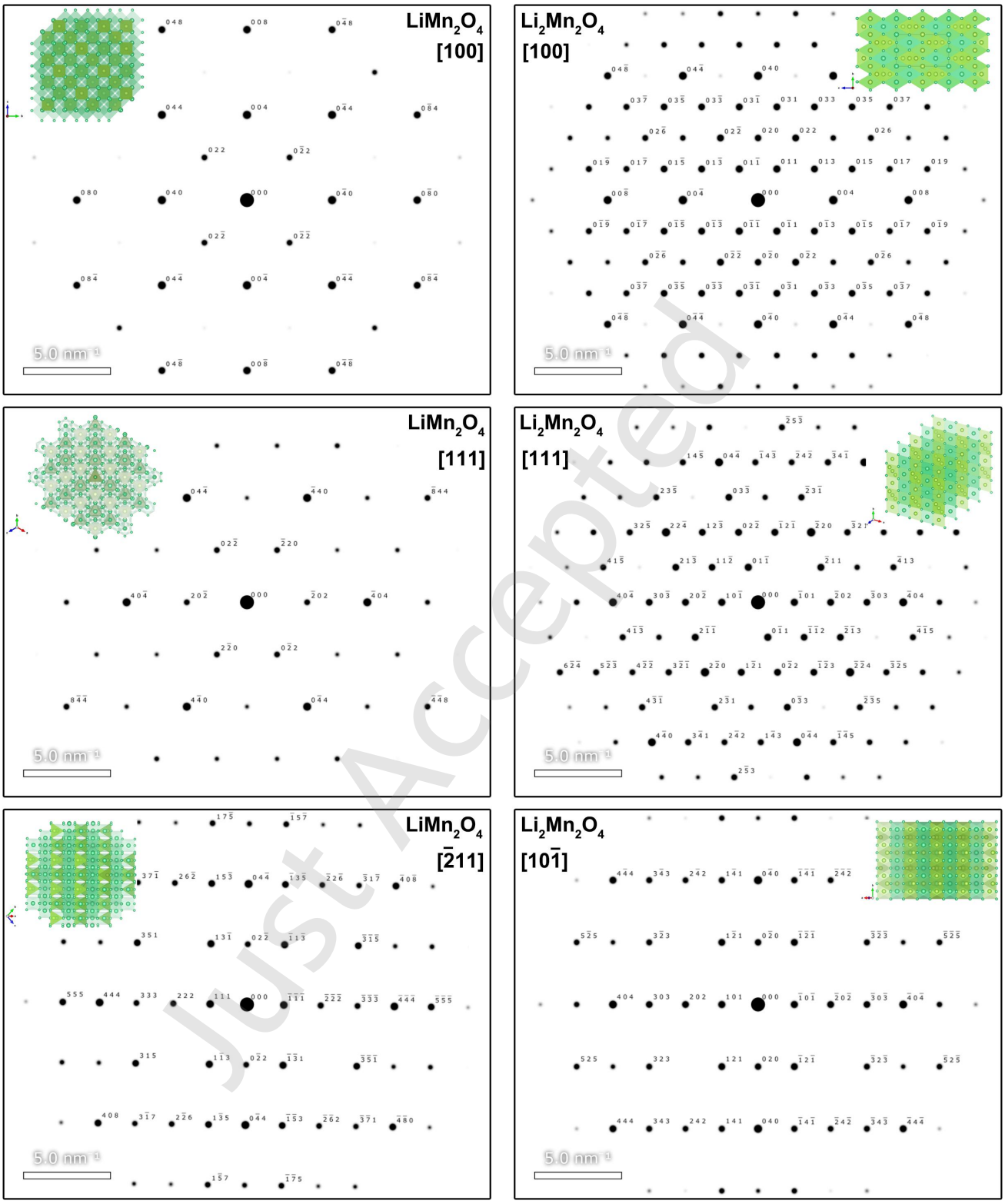

Figure S17. Atomic models and simulated electron diffraction patterns of spinel-phase $LiMn_2O_4$ and rock-salt-phase $Li_2Mn_2O_4$ along different zone axes.

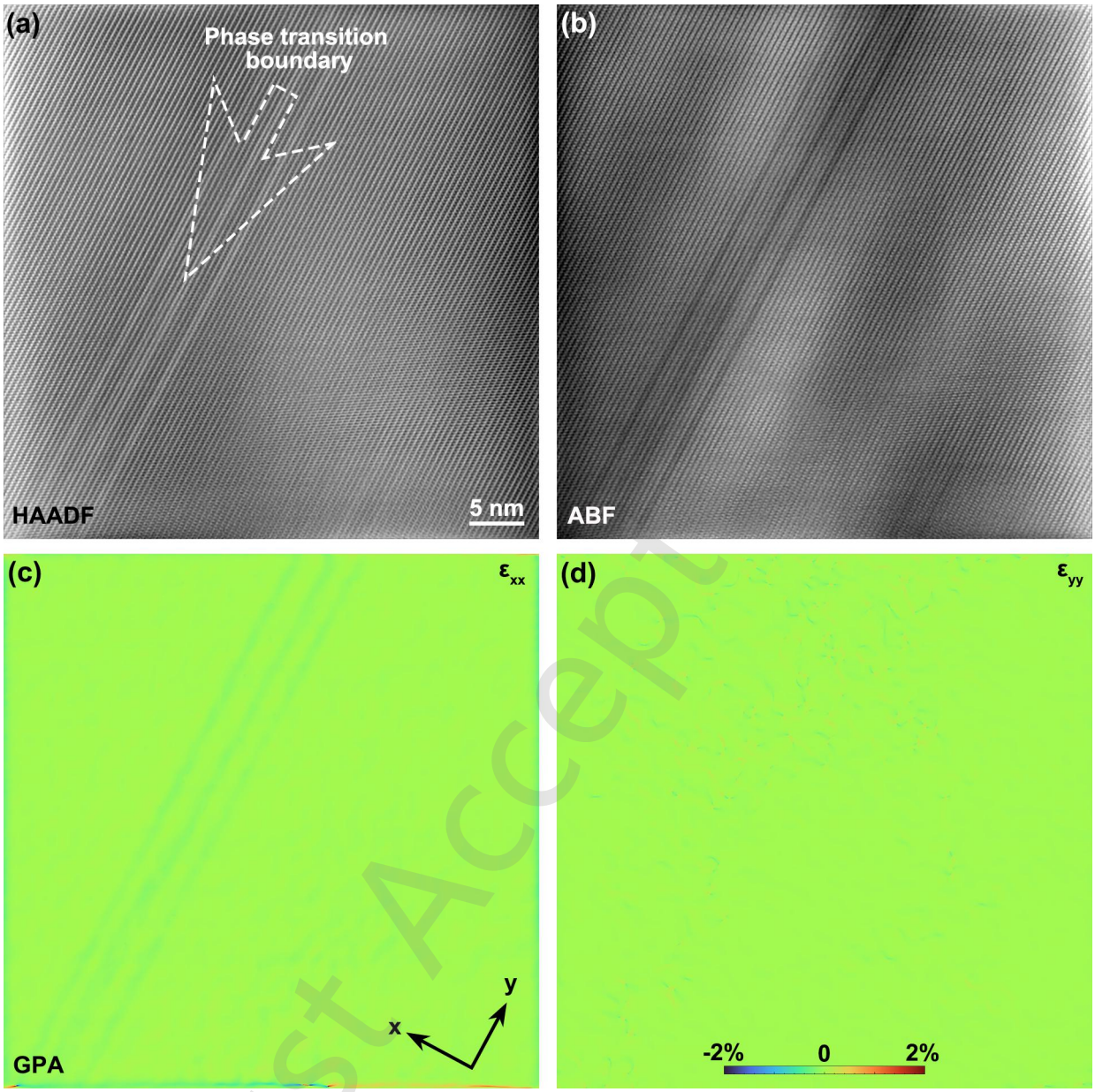

Figure S18. GPA strain maps of LMO in catholyte-based composite cathode.

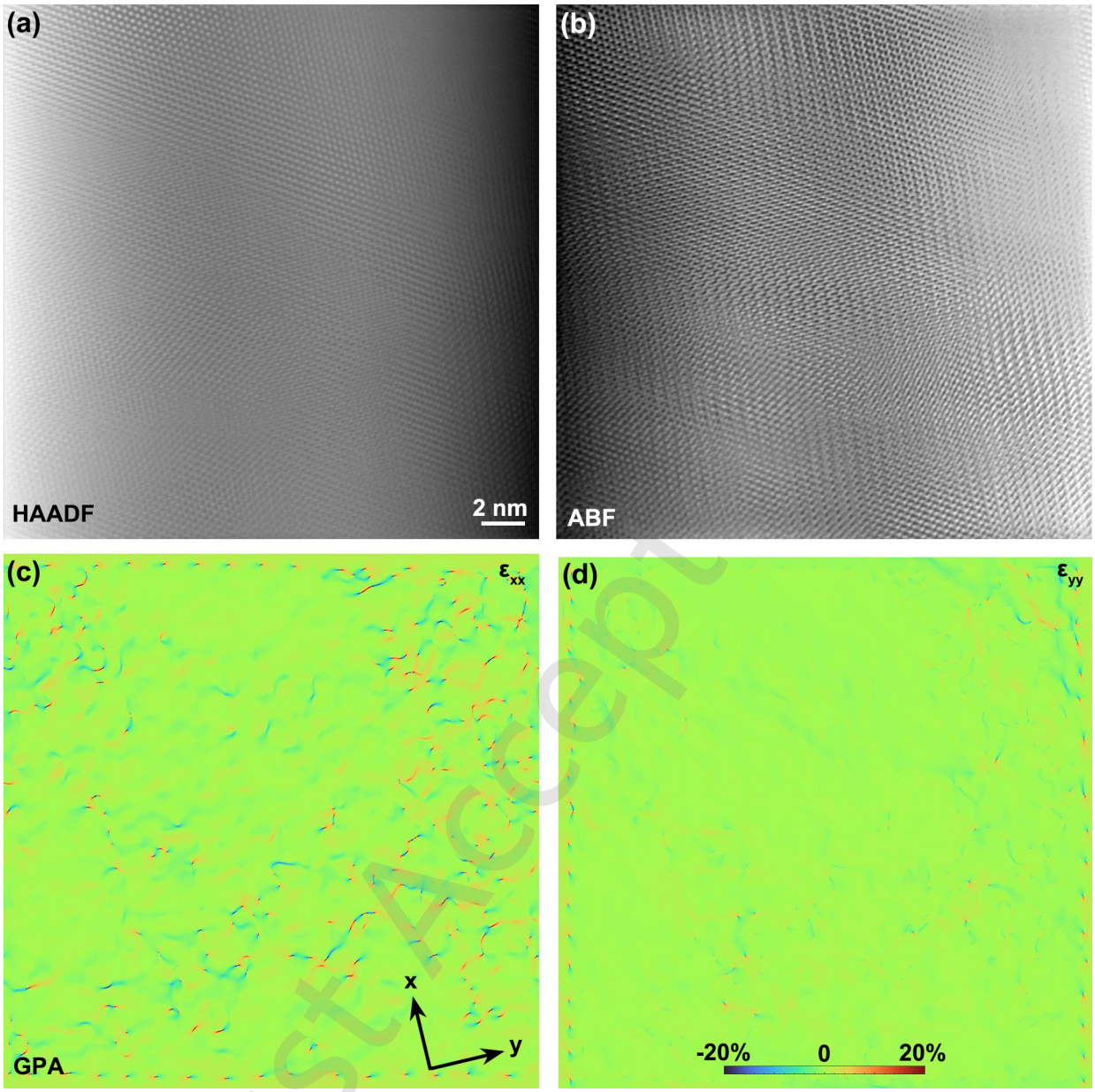

Figure S19. GPA strain maps of LMO in catholyte-free composite cathode.

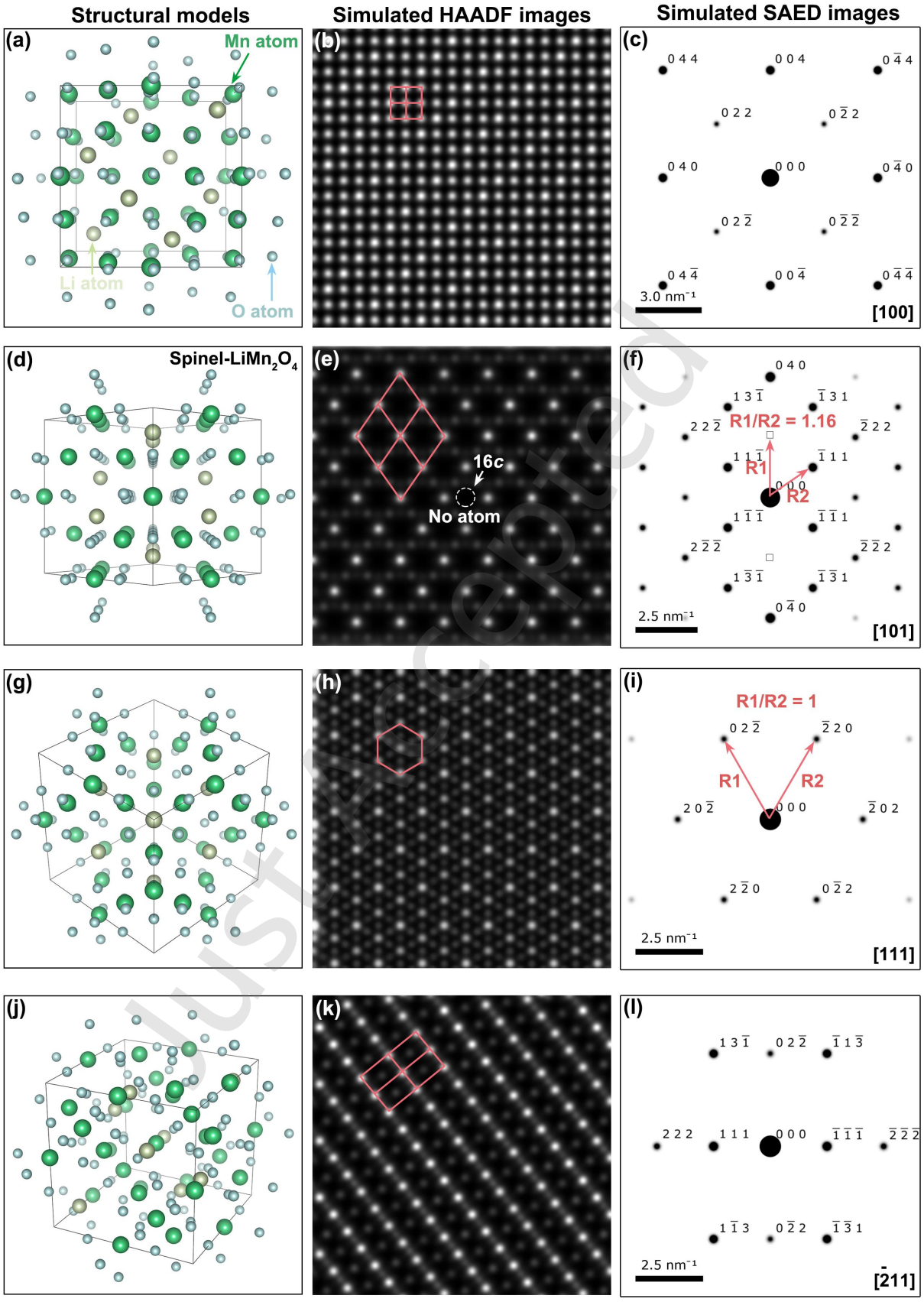

Figure S20. The structural models of spinel-phase LMO viewed along different zone axes and the corresponding simulated HAADF images and SAED images.

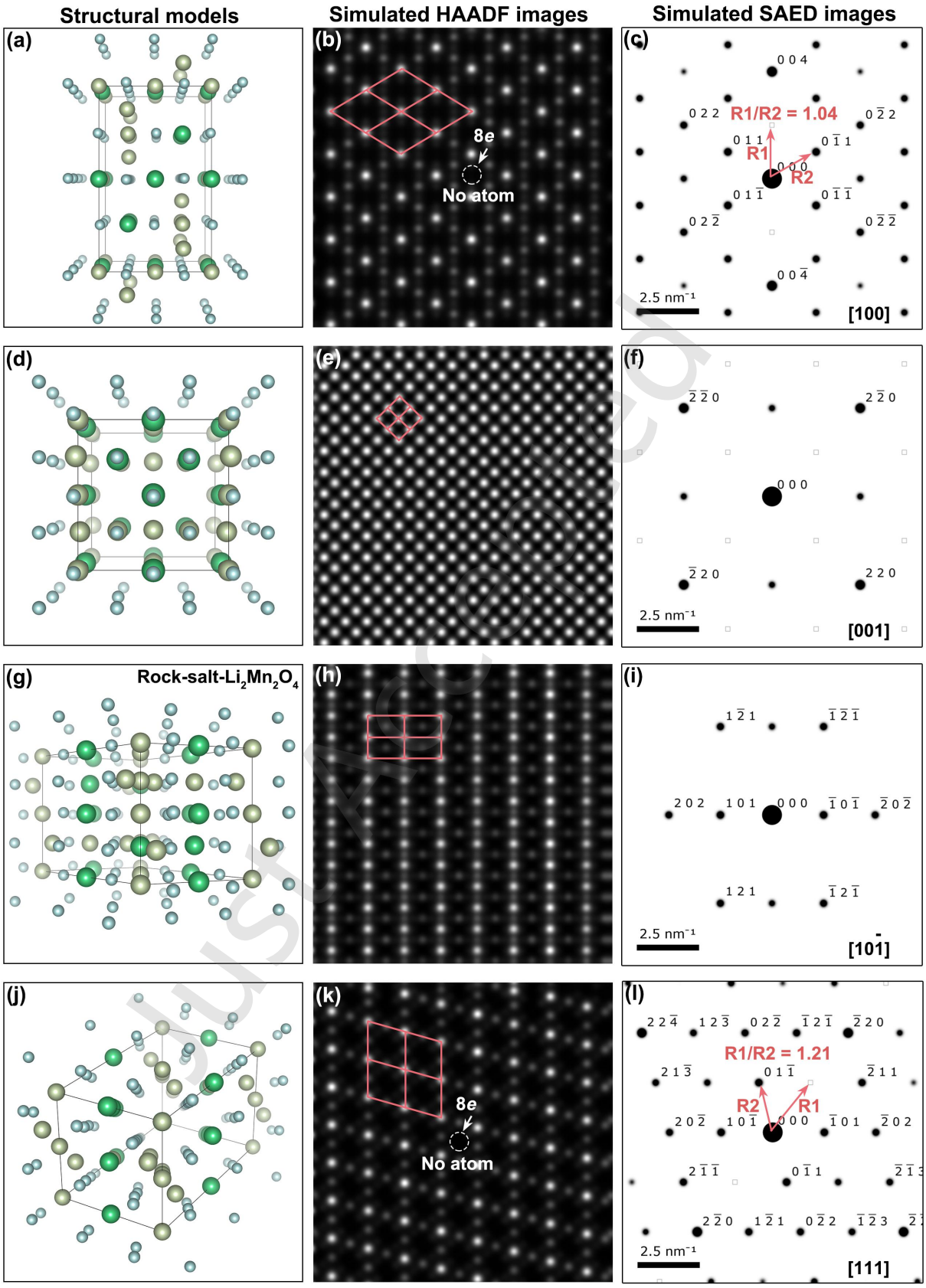

Figure S21. The structural models of rock-salt-phase $Li_2Mn_2O_4$ viewed along different zone axes and the corresponding simulated HAADF images and SAED images.

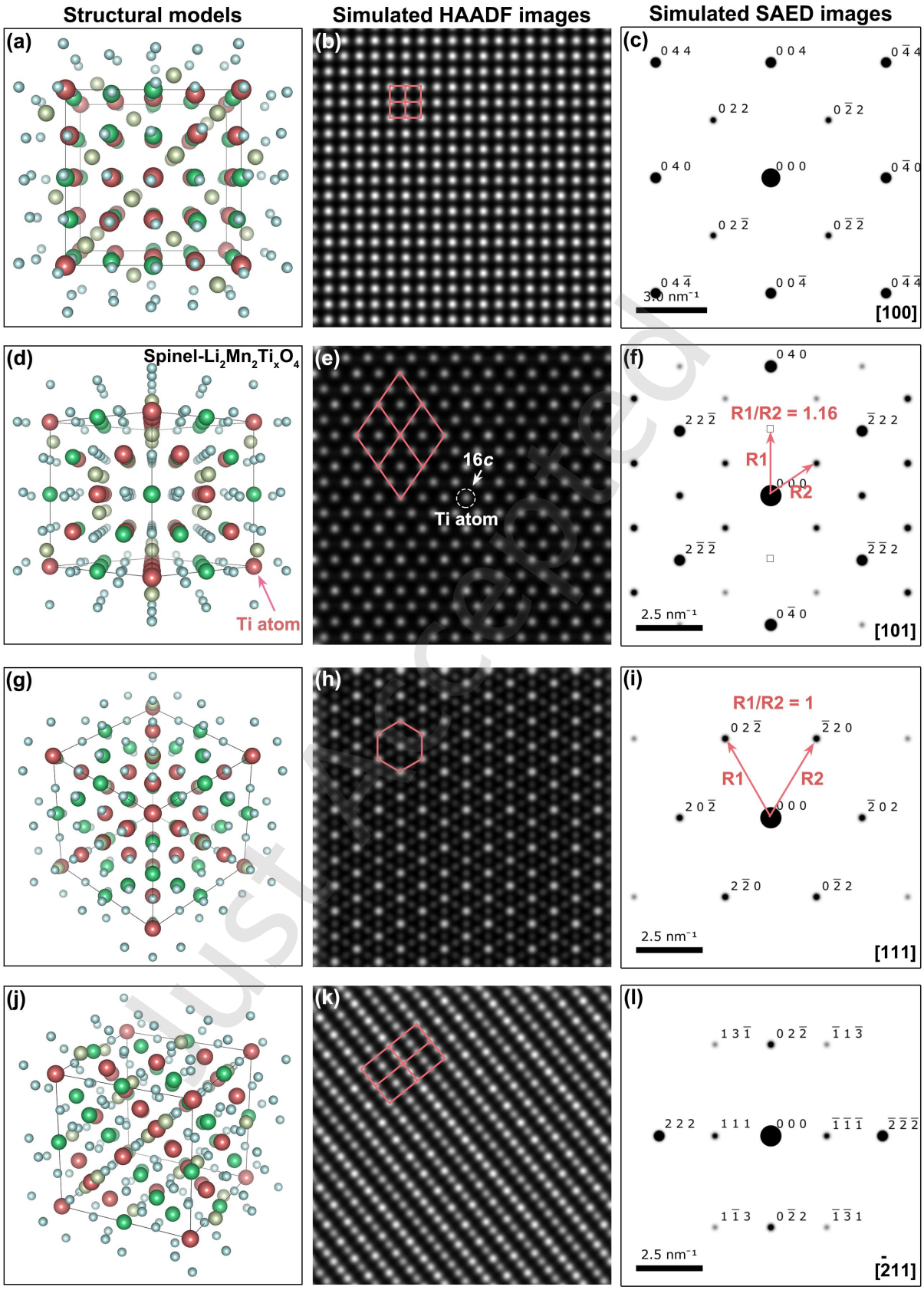

Figure S22. The structural models of spinel-phase $Li_2Mn_2Ti_xO_4$ viewed along different zone axes and the corresponding simulated HAADF images and SAED images.

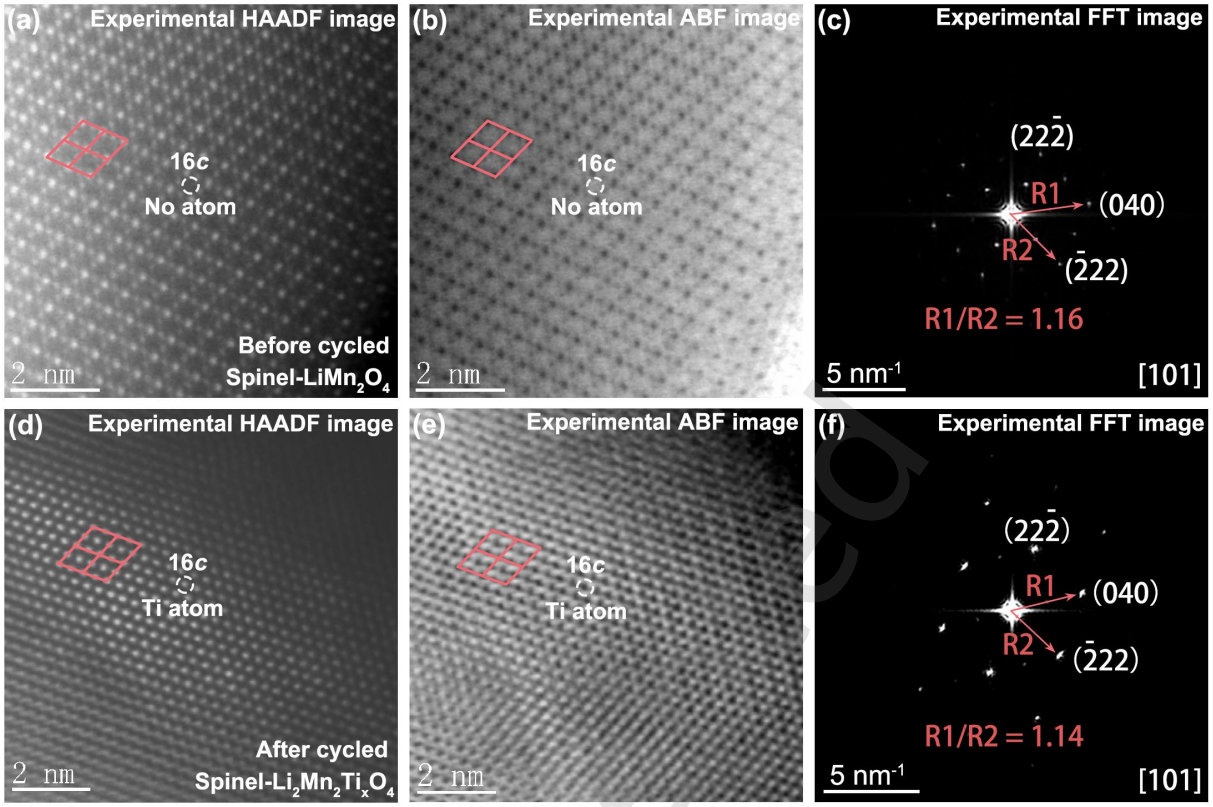

Figure S23. HAADF (a), ABF (b), and FFT (c) images of spinel-phase LMO before cycled. HAADF (d), ABF (e), and FFT (f) images of spinel-phase $Li_2Mn_2Ti_xO_4$ after cycled.

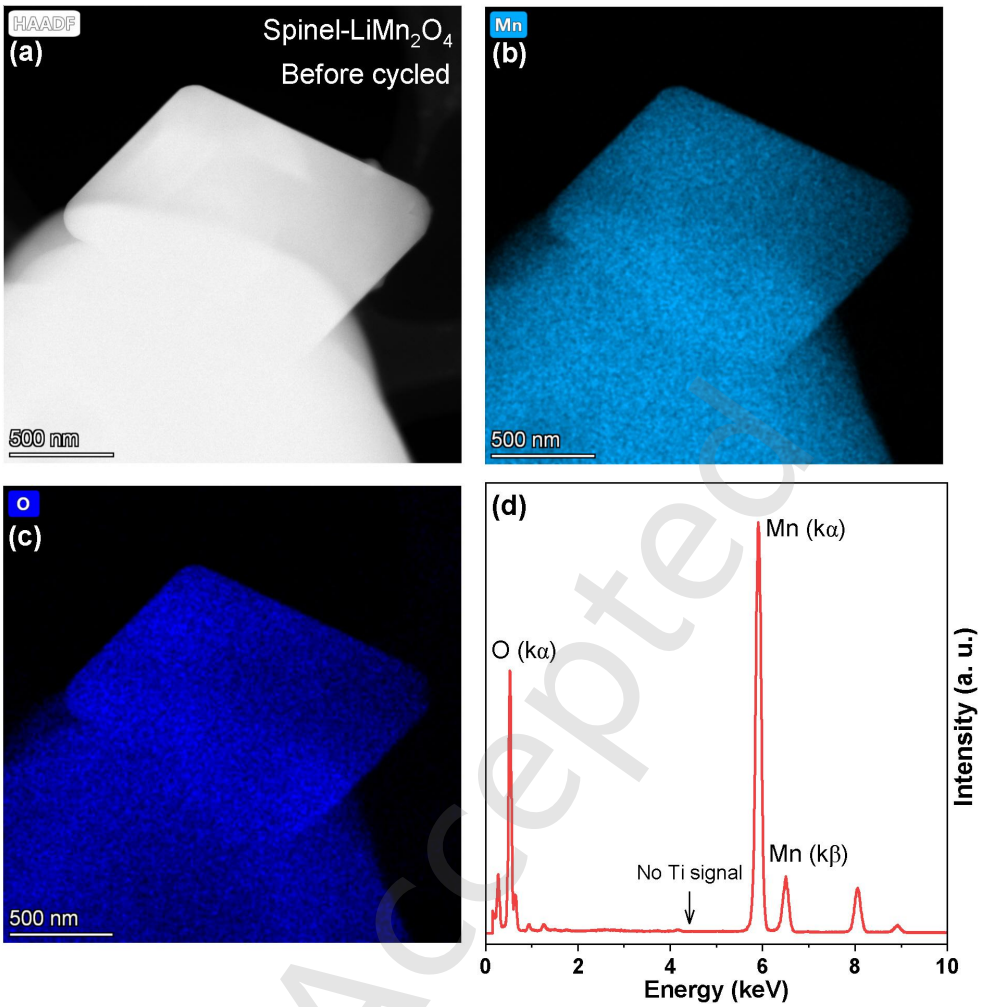

Figure S24. EDS results of $LiMn_2O_4$ before cycled.

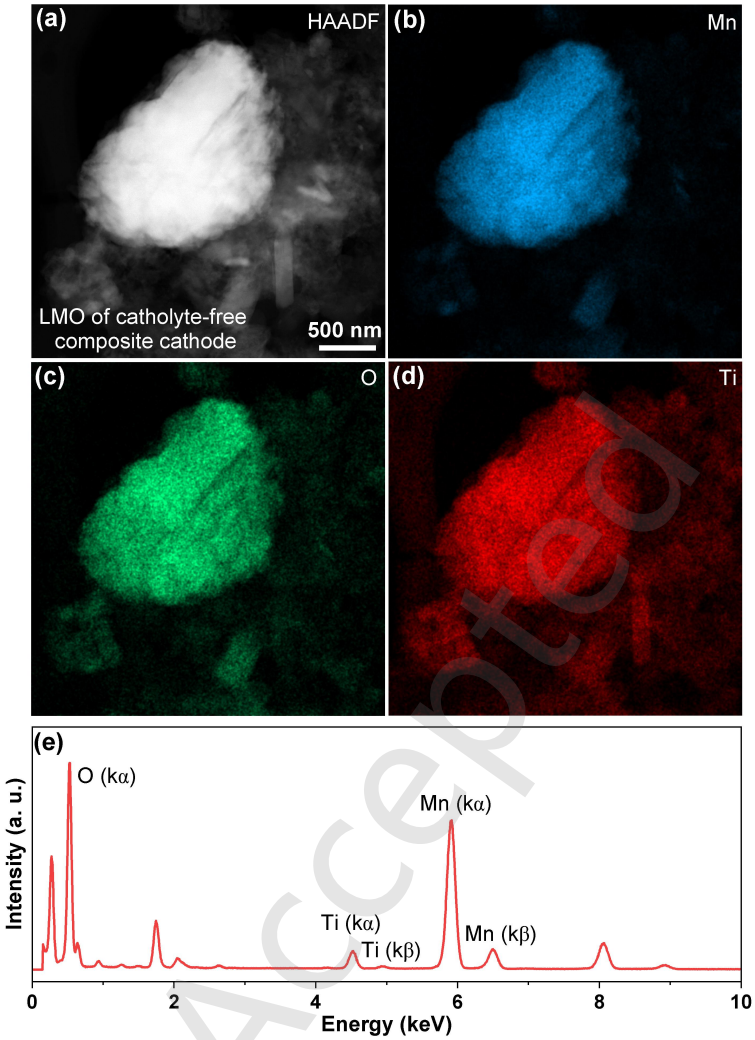

Figure S25. EDS results of $Li_2Mn_2Ti_xO_4$ after cycled.

Table S1. Rietveld refinement result from the XRD data of the LMO. The space group is $Fd\bar{3}m$. The refined lattice parameters are $a = b = c = 8.21097(11)$ Å, $\alpha = \beta = \gamma = 90^{\circ}$. The unit-cell volume is 553.583(21) Å^3.

Atoms	x	y	z	Occ.	site	Sym.	U_{iso} (Å^2)
Li	0.125	0.125	0.125	1	8*a*	-43m	0.0190(7)
Mn	0.5	0.5	0.5	1	16*d*	-3m	0.0094(5)
O	0.26176(28)	0.26176(28)	0.26176(28)	1	32*e*	3m	0.0142(12)

Table S2. Rietveld refinement result from the XRD data of the LTC. The space group is *C2/m*. The refined lattice parameters are a = 6.3102(19) Å, b = 10.9043(6) Å, c = 6.3229(19) Å, α = γ = 90°, and β = 109.788(5)°. The unit-cell volume is 409.377(14) Å^3.

Atoms	x	y	z	Occ.	site	Sym.	U_{iso} (Å^2)
Li1	0	0.170(5)	1/2	1	4*h*	2	0.122(9)
Li2	1/2	0	1/2	1	2*d*	2/m	0.122(9)
Ti1	0	0	0	0.762(4)	2*a*	2/m	0.0021(7)
Ti2	0	0.3325(19)	0	0.1190(22)	4*g*	2	0.0021(7)
Cl1	0.2385(5)	0.15859(23)	0.2388(4)	1	8*j*	1	0.01733(29)
Cl2	0.2400(7)	0	-0.2294(7)	1	4*i*	m	0.01733(29)

Table S3. Effect of the ratio of two active materials in a catholyte-free composite cathode on the theoretical energy density.

	Nominal Capacity (mAh/g)	Molecular Weight (g/mol)	Material Density (g/cm^3)	Gravimetric energy densities (Wh/kg)
LMO	108.00	176.02	4.23	270.30
LTC	95.20	281.40	2.18	/
LMO:LTC=50:50	101.60	228.71	3.21	305.27
LMO:LTC=55:45	102.24	223.44	3.31	306.88
LMO:LTC=60:40	102.88	218.17	3.41	308.75
LMO:LTC=65:35	103.52	212.90	3.51	310.35
LMO:LTC=70:30	104.16	207.63	3.62	312.22
LMO:LTC=75:25	104.80	202.37	3.72	314.07
LMO:LTC=80:20	105.44	197.10	3.82	315.67
LMO:LTC=85:15	106.08	191.83	3.92	317.52
LMO:LTC=90:10	106.72	186.56	4.03	319.12

Table S4. All-solid-state lithium pouch batteries design parameters input in SolidPAC software.

Name	catholyte-based composite cathodes	catholyte-free composite cathodes
Active material fraction (wt%)	70	95
Catholyte fraction (wt%)	25	0
Carbon fraction (wt%)	3	3
Binder fraction (wt%)	2	2
Cathode porosity (%)	5	5
Cathode areal loading (mAh cm^{-2})	6	6
Catholyte selection	Li_2ZrCl_6	Li_3TiCl_6
Anode selection	Li	
N/P ratio	1.2	
Electrolyte selection	Li_2ZrCl_6	
Electrolyte thickness	25 μm	
Stacking selection	Conventional stacking	
Al CC Thickness (μm)	15	
Cu CC Thickness (μm)	10	
Cell design parameters	Default values	

Table S5. Material parameters input in SolidPAC software.

	Catholyte-based composite cathode inputs		Catholyte-free composite cathodes inputs	Anode inputs
Name	LMO		LMO+LTC	Li
Nominal Capacity (mAh/g)	108		316.3	3860
Molecular Weight (g/mol)	176.02		176.02	6.94
Material Density (g/cm^3)	4.23		4.23	0.534
OCV at 20% SOC, V	4.06		3.04	/
OCV at 50% SOC, V	4.14		3.78	/
OCV at 80% SOC, V	4.23		4.06	/
OCV at 100% SOC, V	4.3		4.32	/
Solid state electrolyte inputs				
Name	LiPON	$0.6Li_2B_{12}H_{12}$-0.4LiI	Ga-LLZO	PVDF-HFP/LiTFSI-$Li_{1.2}Y_{0.2}Zr_{1.8}(PO_4)_3$	$Li_{2.5}Lu_{0.5}Zr_{0.5}Cl_6$
Lithium Availability (g/g of electrolyte)	0.1798	0.0743	0.0579	0.05	0.0478
Molecular Weight (g/mol)	115.79	146.9	839.74	265.65	363.15
Material Density (g/cm^3)	2.3	2.36	5.2	1.9	2.8
Conductivity (mS/cm)	1	1	0.5	1	1
Anode | SE Interfacial Resistance (Ω cm^2)	50	100	100	100	100
Cathode | SE Interfacial Resistance (Ω cm^2)	500	200	200	200	200
Name	Li_3InCl_6	$Li_7La_3Zr_2O_{12}$	LAGP-PEO(LiTFSI)	Li_6PS_5Cl	$Li_{0.35}La_{0.55}TiO_3$
Lithium Availability (g/g of electrolyte)	0.0598	0.0579	0.0247	0.1551	0.0139
Molecular Weight (g/mol)	348.35	839.74	416.45	268.4	174.69
Material Density (g/cm^3)	2.59	5.2	2.9	1.54	5
Conductivity (mS/cm)	1	0.5	1	1	0.1
Anode | SE Interfacial Resistance (Ω cm^2)	50	100	100	50	100
Cathode | SE Interfacial Resistance (Ω cm^2)	200	200	200	200	500
Name	Li_2ZrCl_6	Li_3TiCl_6			
Lithium Availability (g/g of electrolyte)	0.0437	0.0740			
Molecular Weight (g/mol)	317.8	281.4			
Material Density (g/cm^3)	2.56	2.18			
Conductivity (mS/cm)	1	1			
Anode | SE Interfacial Resistance (Ω cm^2)	50	50			
Cathode | SE Interfacial Resistance (Ω cm^2)	200	200			

Table S6. Recent publications on the configuration and energy density estimation of all-solid-state lithium pouch batteries.

Solid-state electrolytes	Cathode loading (wt%)	Voltage range (V vs. Li/Li^+)	Initial discharge capacity (mAh g^{-1})	Gravimetric volumetric energy densities (Wh kg^{-1})	Volumetric energy densities (Wh L^{-1})	Temperature (°C)	Year	Refs.
LiPON	~80	3.2-4.4	122	340.5	885.5	25	2025	Xia et. al.[1]
$0.6Li_2B_{12}H_{12}$-0.4LiI (Li3InCl6)	70	2.5-4.2	132	324.1	866.7	60	2025	Xu et. al.[2]
Ga-LLZO	80	3.0-4.5	105	273.3	885.5	25	2024	Ghosh et.al.[3]
PVDF-HFP/LiTFSI-$Li_{1.2}Y_{0.2}Zr_{1.8}(PO_4)_3$	~70	3.5-4.4	104	265.9	733.3	25	2024	Gami et. al.[4]
$Li_{2.5}Lu_{0.5}Zr_{0.5}Cl_6$	70	3.0-4.3	119.4	292.8	828.9	RT	2023	Wang et. al.[5]
Li_3InCl_6	51	3.4-4.3	98	186	616.4	/	2023	Hendriks et. al.[6]
$Li_7La_3Zr_2O_{12}$	80	3.0-4.5	104.3	271.8	885.5	/	2023	Ghosh et. al.[7]
LAGP-PEO(LiTFSI)	80	3.0-4.3	100	281.4	847.8	30	2021	Wang et. al.[8]
Li_6PS_5Cl	38	3.3-4.5	73	107.8	311.5	RT	2017	Auvergniot et. al.[9]
$Li_{0.35}La_{0.55}TiO_3$	80	3.0-4.3	82	224.4	790.8	25	2009	Hara et. al.[10]
Li_2ZrCl_6	70	2.92-4.32	107.7	**269.6**	**790.8**	25	2026	**This Work**
Li_2ZrCl_6	70	2.32-4.32	180.5	**404.1**	**930.6**	25	2026	**This Work**
Li_3TiCl_6	70	2.92-4.32	136.5	**302.7**	**780.03**	25	2026	**This Work**
Li_3TiCl_6	70	2.02-4.32	316.4	**588.8**	**1019.6**	25	2026	**This Work**
Li_3TiCl_6	70	1.62-4.32	374.7	**670.0**	**1080.1**	25	2026	**This Work**

Table S7. Differences in calculating the theoretical energy density when considering only the mass of the oxide active material versus the mass of the entire composite cathode.

	Catholyte-based composite cathode (LMO+LZC)		Catholyte-free composite cathodes (LMO+LTC)	
	mAh/g_{LMO}	$mAh/g_{composite\ cathode}$	mAh/g_{LMO}	$mAh/g_{composite\ cathode}$
Nominal Capacity (mAh/g)	108.00	75.50	148.9	104.16
Molecular Weight (g/mol)	176.02	213.34	176.02	207.63
Material Density (g/cm^3)	4.23	3.79	4.23	3.62
Active material fraction (wt%)	70	95	70	95
Catholyte fraction (wt%)	25	0	25	0
Carbon fraction (wt%)	3			
Binder fraction (wt%)	2			
Cathode porosity (%)	5			
Cathode areal loading (mAh/cm^2)	6			
Gravimetric energy densities (Wh/kg)	270.26	258.22	325.99	312.22
Volumetric energy density (Wh/L)	790.83	790.83	814.83	814.83

Table S8. Calculating the theoretical energy density when considering only the mass of the oxide active material versus the mass of the entire composite cathode.

	SOC=20%	SOC=50%	SOC=80%	SOC=100%	mAh/g_{LMO}	Wh/kg	Wh/L	mAh/$g_{composite\ cathode}$	Wh/kg	Wh/L
Catholyte-based composite cathode (LMO+LZC)										
2.92-4.32	4.06	4.14	4.23	4.32	107.70	269.61	790.83	75.39	257.89	790.83
2.32-4.32	3.01	4.00	4.15	4.32	180.50	404.14	930.59	126.35	387.82	930.59
Catholyte-free composite cathodes (LMO+LTC)										
2.92-4.32	3.04	3.78	4.06	4.32	136.40	302.70	780.03	95.5	289.78	780.03
2.02-4.32	3.04	3.78	4.06	4.32	316.40	588.80	1019.62	221.48	567.81	1019.62
1.62-4.32	3.07	3.82	4.09	4.32	374.70	669.97	1080.05	262.29	647.18	1080.05

References

[1] Q. Xia, X. Lei, F. Yue, W. Liu, C. Xu, J. Xu, M. Yang, X. Huang, D. Su, H. Xia, Unraveling the $LiMn_2O_4$/LiPON interface degradation in all-solid-state thin-film lithium batteries, *Nano Lett.* **2025**, *25*, 7892.

[2] D. Xu, M. Jin, Z. Su, R. Liu, M. Xiang, W. Fang, L. He, R. Wu, Y. Guo, Facile synthesis of inorganic $Li_2B_{12}H_{12}$/LiI solid electrolytes for high‐voltage all‐solid‐state lithium batteries, *Adv. Sci.* **2025**, *12*, e10193.

[3] K. Ghosh, M. Wasim Raja, Facile Li-ion transport in microstructurally engineered hybrid LLZO electrolyte for application in pseudo-solid state lithium metal batteries, *Chem. Eng. J.* **2024**, *480*, 148200.

[4] P. Gami, M. Badole, H. N. Vasavan, A. K. Das, S. Saxena, S. Kumar, Y-doped $LiZr_2(PO_4)_3$ in a PVDF-HFP composite electrolyte for solid-state Li-metal batteries, *ACS Appl. Eng. Mater.* **2024**, *2*, 1278.

[5] C. Wang, S. Wang, X. Liu, Y. Wu, R. Yu, H. Duan, J. T. Kim, H. Huang, J. Wang, Y. Mo, X. Sun, New insights into aliovalent substituted halide solid electrolytes for cobalt-free all-solid state batteries, *Energy Environ. Sci.* **2023**, *16*, 5136.

[6] T. A. Hendriks, M. A. Lange, E. M. Kiens, C. Baeumer, W. G. Zeier, Balancing partial ionic and electronic transport for optimized cathode utilization of high‐voltage $LiMn_2O_4$/Li_3InCl_6 solid‐state batteries, *Batteries Supercaps* **2023**, *6*, e202200544.

[7] K. Ghosh, M. Wasim Raja, Engineered $Li_7La_3Zr_2O_{12}$ (LLZO) for pseudo-solid-state lithium metal batteries (SSLMBs): Tailor-made synthesis, evolution of the microstructure, suppression of dendritic growth, and enhanced electrochemical performance, *ACS Appl. Energy Mater.* **2023**, *6*, 4035.

[8] C. Wang, G. Bai, X. Liu, Y. Li, Favorable electrochemical performance of $LiMn_2O_4$/$LiFePO_4$ composite electrodes attributed to composite solid electrolytes for all-solid-state lithium batteries, *Langmuir* **2021**, *37*, 2349.

[9] J. Auvergniot, A. Cassel, J.-B. Ledeuil, V. Viallet, V. Seznec, R. Dedryvère, Interface stability of argyrodite Li_6PS_5Cl toward $LiCoO_2$, $LiNi_{1/3}Co_{1/3}Mn_{1/3}O_2$, and $LiMn_2O_4$ in bulk all-solid-state batteries, *Chem. Mater.* **2017**, *29*, 3883.

[10] M. Hara, H. Nakano, K. Dokko, S. Okuda, A. Kaeriyama, K. Kanamura, Fabrication of all solid-state lithium-ion batteries with three-dimensionally ordered composite electrode consisting of $Li_{0.35}La_{0.55}TiO_3$ and $LiMn_2O_4$, *Journal of Power Sources* **2009**, *189*, 485.